Research Square

Preprints are preliminary reports that have not undergone peer review.
They should not be considered conclusive, used to inform clinical practice,
or referenced by the media as validated information.

Finite volume simulations of dynamic brittle fracture using an exponential-based hyperbolic formulation of gradient damage models

Adrien Renaud

adrien.renaud@univ-amu.fr

Institut Universitaire des Systèmes Thermiques Industriels

Thomas Heuzé

Institut de Recherche Dupuy de Lôme

Nicolas Favrie

Institut Universitaire des Systèmes Thermiques Industriels

Research Article

Keywords: Brittle fracture, Dynamic fracture, Gradient damage, Hyperbolic models, Finite volumes, Kalthoff-Winkler test, Crack branching

Posted Date: March 9th, 2026

DOI: https://doi.org/10.21203/rs.3.rs-9009636/v1

License: This work is licensed under a Creative Commons Attribution 4.0 International License.
Read Full License

Additional Declarations: No competing interests reported.

Finite volume simulations of dynamic brittle fracture using an exponential-based hyperbolic formulation of gradient damage models

Adrien Renaud · Thomas Heuzé · Nicolas Favrie

the date of receipt and acceptance should be inserted later

Abstract This study provides a multidimensional extension of the hyperbolic formulation of gradient damage models introduced by Favrie *et al.* in one space dimension, and which allows an efficient explicit numerical solution of dynamics problems. The proposed methodology is based on an "extended Lagrangian approach" developed by one of the authors for the nondissipative and dispersive shallow water equation. By using this strategy, the global minimization problem commonly derived for gradient damage models is recast as a hyperbolic one with purely local source terms. The numerical solution of the governing system of equations is then based on a fractional-step method consisting of a classical Godunov-type finite volume scheme to solve the homogeneous part of the system, followed by an implicit Ordinary Differential Equation solver for the local source terms. Stored-energy functions corresponding to well-known damage models (*i.e.* Ambrosio & Tortorelli or AT models) are used with, however, the introduction of a new *relaxed damage variable* to easily handle damage boundedness. The proposed model is illustrated on two-dimensional test cases: the Kalthoff-Winkler experiment and a crack branching test.

Keywords Brittle fracture · Dynamic fracture · Gradient damage · Hyperbolic models · Finite volumes · Kalthoff-Winkler test · Crack branching

A. Renaud
Laboratoire IUSTI (Aix Marseille University, CNRS UMR 7343), 13453 Marseille, France
ORCid 0000-0002-3075-4933
E-mail: adrien.renaud@univ-amu.fr
Present address: adrien.renaud@ec-nantes.fr

T. Heuzé
Univ Brest, Bretagne INP, Institut de Recherche Dupuy de Lôme (IRDL), UMR CNRS 6027
F-29200, Brest, France
E-mail: thomas.heuze@enib.fr

N. Favrie
Laboratoire IUSTI (Aix Marseille University, CNRS UMR 7343), 13453 Marseille, France
E-mail: nicolas.favrie@univ-amu.fr

1 Introduction

From its early development in the late 50s [23], it has been established that damage mechanics is a very efficient tool to describe the degradation up to failure of a variety of materials. In this formalism, the degradation of material due to the appearance of micro-cracks and/or micro-voids is described by means of an internal variable $\mathcal{D}$ that acts on the stiffness through a monotonically decreasing *degradation function*.

However, it is now well known that local damage models lead to mathematically ill-posed governing equations in the context of boundary value problems that yield non-uniqueness of the solution and spurious damage localization issues [3,4]. This shortcoming of damage mechanics has been addressed by the development of non local regularization. On the one hand, volume averages quantities such as the damage energy release rate [45] or some equivalent strain measures [11,41] have been introduced in the damage evolution problem. Alternatively, the space and time derivatives of the damage field [17] have been considered in free and kinetic energy densities. The introduction of the space derivative of $\mathcal{D}$ in the solid energy proposed in the latter approach paved the way for what is today known as the class of *gradient damage models* for which a variational formulation has been derived [31]. Gradient damage models have later been shown to fit the Generalized Standard Materials (GSM [20]) framework [39,32], and the associated variational formulation can be consistent with fracture mechanics in a Γ-convergence sense [6]. It is worth noticing that the latter reference is often considered as the foundation of phase-field models of fracture [35,5].

Numerical models involving gradient damage models allowed successful finite element simulations of brittle fracture problems in quasi-static [32,2, 35,42,7,51] and in dynamics [5,34,30,18,49], but also, for instance, Material Point Method computations in dynamics [55,54]. Alternatively, brittle fracture problems have been addressed through the Thick Level Set method [38] and the Lip-Field approach [8] which are numerical regularizations of local damage models in a finite element framework and that have also been applied to dynamics [36,37]. In the context of solid dynamics, however, the nature of the Partial Differential Equations (PDEs) derived from gradient damage models can be discussed as pointed out in [33]. Indeed, the non-local regularization leads, in the rate-dependent case, to a parabolic equation for damage evolution that in turn implies infinite wave speeds, as for the heat equation or a Poisson equation. For rate-independent formulations on the other hand, damage evolution closely follows elastic waves which may also be limiting. Therefore, the interest for a hyperbolic formulation of gradient damage models emerged in the late 2010's and appeared through the introduction of damaged-induced inertia [40,25,19], as suggested by Frémond & Nedjar in the quasi-static context [17] twenty years before. Although such formulations make gradient damage wave-consistent, the damage driving force derived from the second principle of thermodynamics is still non-local and involves the Laplacian of the damage field. This in turn makes the discrete non-linear problem associ-

ated with damage evolution non-local which, in an explicit dynamics context, can lead to prohibitive computational times. In addition, computing high order derivatives is not straightforward in finite volume modeling [29], which enables the accurate description of waves owing to plenty of numerical tools developed for computational fluid dynamics. The efficient explicit finite volume solution of solid dynamics problem based on gradient damage models has been made possible [14] by means of the *extended Lagrangian* strategy originaly developped for non dissipative dispersive systems [12, 13]. Using the latter, the original global problem has been recast as a hyperbolic one with purely local source terms that can easily be solved using finite volumes coupled to implicit ODE solvers. The approach being non classical, the author limited themselves to one-dimensional examples [14]. It must be emphasized that the same order of accuracy is achieved for velocity, stress, strain and damage in this finite volume model, which may not be the case in the context of finite element modeling of gradient damage. Although the aforementioned hyperbolic model shows some similarities with the micromorphic formulation [15] of gradient damage including micro-inertia presented in [53], the latter considers a different contribution of damage to micro-inertia and is not well suited to finite volumes.

The present paper is in line with the aforementioned work and provides an extension to multi-dimensional problems taking into account the effect of crack opening/closing while guaranteeing the hyperbolicity of the governing PDEs. This requires the use of a proper tension/compression split of the solid free energy density to distinguish crack opening and crack closure. Another originality of the present work lies in the introduction of a new *relaxed damage variable* $\mathscr{D} \geq 0$ to deal with the bound $0 \leq \mathcal{D} < 1$ without external constraint and/or additional penalty terms.

The paper is organized as follows, the thermodynamical formulation of the classical gradient damage model is recalled in section 2. Section 3 is devoted to the derivation of the hyperbolic model using Hamilton's principle completed by a thermodynamically-consistent dissipative potential. In particular, we put emphasis on the straightforward treatment of damage boundedness by means of a new relaxed damage variable in section 3.2.

The Riemann problem is analyzed in section 4 and unconditional hyperbolicity is proved for the hydrostatic/deviatoric split of the free energy density assumed to take into account unilateral effects due to crack closure. Next, the considered finite volume scheme embedding approximate Riemann solvers with high order fluxes is detailed in section 5. Numerical results are presented in Section 6. A parametric analysis is first performed on a one-dimensional multi-fragmentation test in section 6.1, and the proposed model is illustrated on the well-known Kalthoff-Winkler experiment in section 6.2. Furthermore, the ability to describe crack branching is shown on a symmetric tensile problem in a pre-notched rectangular specimen in section 6.3. Conclusion and perspectives are provided in section 7.

2 Constitutive model

The modeling of brittle fracture by means of nonlocal damage model following Colleman & Noll's procedure under small strains is commonly constructed upon Helmholtz's free energy density that is additively decomposed into elastic and damage stored energy parts according to:

$$\Psi(\boldsymbol{\varepsilon}, \mathcal{D}) = \psi^e(\boldsymbol{\varepsilon}, \mathcal{D}) + \psi^d(\mathcal{D}, \boldsymbol{\nabla}\mathcal{D}), \tag{1}$$

where $\boldsymbol{\varepsilon}$ is the linearized strain tensor and $\mathcal{D} \in [0, 1]$ is the damage field conjugate to the thermodynamic force whose definition is based on the following variational derivative:

$$\mathsf{Y}_{\mathcal{D}} = div\, \frac{\partial \Psi}{\partial \boldsymbol{\nabla}\mathcal{D}} - \frac{\partial \Psi}{\partial \mathcal{D}} \tag{2}$$

2.1 Damage energy density

Nonlocal damage models can furthermore be related to Griffith's theory by means of a *crack surface density function* γ_{ℓ_0} [35]:

$$\int_\Omega \psi^d(\mathcal{D}, \boldsymbol{\nabla}\mathcal{D}) dV = \int_\Omega G_c \gamma_{\ell_0}(\mathcal{D}, \boldsymbol{\nabla}\mathcal{D}) dV = \Gamma_c G_c, \tag{3}$$

in which G_c is the material fracture toughness and Γ_c the discrete crack surface.

A widely used form of the crack density function [2,35,7,34,30,5] is that derived from the work of Ambrosio and Tortorelli [1], applied to fracture mechanics in [6], and which led to the so-called *AT models*:

$$\gamma_{\ell_0}(\mathcal{D}, \boldsymbol{\nabla}\mathcal{D}) = \frac{1}{4\ell_0 c_w} \left(w(\mathcal{D}) + \ell_0^2 \left\| \boldsymbol{\nabla}\mathcal{D} \right\|^2 \right), \tag{4}$$

with $c_w = \int_0^1 \sqrt{w(s)} ds$ a normalization parameter. In particular, the forms $w(\mathcal{D}) = \mathcal{D} \rightarrow c_w = 2/3$ and $w(\mathcal{D}) = \mathcal{D}^2 \rightarrow c_w = 1/2$ yield the AT1 and AT2 models respectively.

Remark 1 In [5], the crack surface density function is defined with the characteristic length ℓ_c as:

$$\gamma_{\ell_c}(\mathcal{D}, \boldsymbol{\nabla}\mathcal{D}) = \left(\frac{\mathcal{D}^2}{4\ell_c} + \ell_c \left\| \boldsymbol{\nabla}\mathcal{D} \right\|^2 \right), \tag{5}$$

which is consistent with the AT2 model, provided that $\ell_0 = 2\ell_c$.

It is worth noticing that the model of Frémond & Nedjar [17], which significantly motivated the present work, can be written consistently with AT models. Indeed, the damage part of Helmholtz's free energy density considered in this model can be written as:

$$\psi^d(\mathcal{D}, \boldsymbol{\nabla}\mathcal{D}) = w(\mathcal{D}) + \frac{1}{2}\mathsf{w}_{l_c} l_c^2 \left\| \boldsymbol{\nabla}\mathcal{D} \right\|^2 = w_l \mathcal{D}^p - M_l \left[\log(1 - \mathcal{D}) + \mathcal{D} \right] + \frac{1}{2}\mathsf{w}_{l_c} l_c^2 \left\| \boldsymbol{\nabla}\mathcal{D} \right\|^2, \tag{6}$$

in which w_l, M_l and $\mathsf{w}_{l_c} l_c^2$ are positive parameters related to the initial damage threshold, "damage hardening", and nonlocal effects respectively. Therefore, using the particular values $w_l = \frac{G_c}{4\ell_0 c_w}$ and $\mathsf{w}_{l_c} l_c^2 = \frac{G_c \ell_0}{2c_w}$, one has the damage part of the free energy density:

$$\psi^d(\mathcal{D}, \boldsymbol{\nabla}\mathcal{D}) = G_c \gamma_{\ell_0} - M_l \left[\log(1-\mathcal{D}) + \mathcal{D}\right] \tag{7}$$

Remark 2 The logarithmic term of FRÉMOND & NEDJAR's formulation can be used as a penalty term in order to enforce the boundedness of the damage variable $\mathcal{D}$. The bounded character of the energy maintains $D < 1$ in order to prevent $\log(1-\mathcal{D}) \to \infty$.

A new formulation of damage is proposed in section 3.2 in order to numerically take into account $\mathcal{D} \in [0, 1[$ without additional constraint.

2.2 Elastic energy density

Let us consider the isochoric/volumetric additive split:

$$\psi^e(\mathcal{D}, \boldsymbol{\varepsilon}) = \psi^e_{iso}(\mathcal{D}, \boldsymbol{\varepsilon}) + \psi^e_{vol}(\mathcal{D}, \boldsymbol{\varepsilon}) \tag{8}$$

In order to account for unilateral effects with total recovery of elastic stiffnesses due to cracks closure, the volumetric part of the energy only involves the damage variable through some degradation function $A(\mathcal{D})$ when $\mathrm{tr}\,(\boldsymbol{\varepsilon}) > 0$ (*i.e.* in tension) proposed in [10] and introduced in damage mechanics in [2]:

$$\psi^e(\mathcal{D}, \boldsymbol{\varepsilon}) = \mu A(\mathcal{D})^{iso} \boldsymbol{\varepsilon}^D : \boldsymbol{\varepsilon}^D + \frac{\kappa}{2}\left(A(\mathcal{D})^{vol} \langle \mathrm{tr}\,(\boldsymbol{\varepsilon})\rangle_+^2 + \langle \mathrm{tr}\,(\boldsymbol{\varepsilon})\rangle_-^2\right), \tag{9}$$

where $\boldsymbol{\varepsilon}^D$ is the isochoric part of the infinitesimal strain tensor, μ and κ are the shear and bulk modulii, and $\langle \bullet \rangle_+$ and $\langle \bullet \rangle_-$ denote the positive and negative part functions respectively.

Another writing of this energy density is based on Kelvin's form of the linear elastic constitutive model [16]:

$$\begin{aligned}\psi^e(\mathcal{D}, \boldsymbol{\varepsilon}) &= \boldsymbol{\varepsilon} : \left(\mu A(\mathcal{D})^{iso} \mathbb{P}^D + \frac{3\kappa}{2}\left[A(\mathcal{D})^{vol} \mathbf{1}_{\mathbb{R}^{+,*}}(\mathrm{tr}\,(\boldsymbol{\varepsilon})) + \mathbf{1}_{\mathbb{R}^-}(\mathrm{tr}\,(\boldsymbol{\varepsilon}))\right] \mathbb{P}^H\right) : \boldsymbol{\varepsilon} \\ &= \begin{cases} \frac{1}{2}\boldsymbol{\varepsilon} : \mathbb{C}^+(\mathcal{D}) : \boldsymbol{\varepsilon} \text{ if } \mathrm{tr}\,(\boldsymbol{\varepsilon}) \geq 0 \\ \frac{1}{2}\boldsymbol{\varepsilon} : \mathbb{C}^-(\mathcal{D}) : \boldsymbol{\varepsilon} \text{ if } \mathrm{tr}\,(\boldsymbol{\varepsilon}) < 0 \end{cases}\end{aligned} \tag{10}$$

where $P^H_{ijkl} = \frac{1}{3}\delta_{ij}\delta_{kl}$ is the hydrostatic projector, $P^D_{ijkl} = \frac{1}{2}\left(\delta_{ik}\delta_{jl} + \delta_{il}\delta_{jk}\right) - P^H_{ijkl}$ is the deviatoric projector, δ_{ij} being Kronecker delta symbol, and $\mathbf{1}_E(y)$ is the indicator function:

$$\mathbf{1}_E(y) = \begin{cases} 1 \text{ if } y \in E \\ 0 \text{ if } y \notin E \end{cases} \tag{11}$$

According to the previous definition, the fourth-order elasticity tensor is $\mathbb{C}^+ = 2\mu A(\mathcal{D})^{iso}\mathbb{P}^D + 3\kappa A(\mathcal{D})^{vol}\mathbb{P}^H$ in tension and $\mathbb{C}^- = 2\mu A(\mathcal{D})^{iso}\mathbb{P}^D + 3\kappa\mathbb{P}^H$ in compression, and conserves minor and major symmetries.

Without loss of generality, the same *degradation function* is considered for the isochoric and volumetric parts, namely $A(\mathcal{D})^{iso} = A(\mathcal{D})^{vol} = A(\mathcal{D})$. This function must satisfy the following conditions:

1. $A(\mathcal{D})$ is a monotonically decreasing function of the damage measure,
2. $A(0) = 1$ in the undamaged material,
3. $A(1) = 0$ in the fully damaged material.

Simple polynomial forms of $A(\mathcal{D})$ are usually considered in the literature, namely $A(\mathcal{D}) = (1-\mathcal{D})^n$ with for instance $n = 1$ in [17] and $n = 2$ in [2,35].

2.3 Dual dissipation pseudo-potential

We suppose the existence of a dissipation pseudo-potential $\varphi(\dot{\mathcal{D}})$, the over dot denoting a time partial derivative, and its Legendre transform known as the dual dissipation pseudo-potential $\varphi^*(\mathsf{Y}_\mathcal{D})$ positive, containing the zero, and convex with respect to the damage driving force. One thus writes:

$$\mathsf{Y}_\mathcal{D} = \frac{\partial\varphi}{\partial\dot{\mathcal{D}}} \quad ; \quad \frac{\partial\mathcal{D}}{\partial t} = \frac{\partial\varphi^*}{\partial\mathsf{Y}_\mathcal{D}} \tag{12}$$

3 Derivation of the hyperbolic model

3.1 Extended Lagrangian

Fully hyperbolic equations of dynamic brittle fracture using gradient damage models as those mentioned above have been derived in [14] owing to Hamilton's variational principle based on an *extended Lagrangian*. This derivation was on the one hand inspired by the work of Frémond & Nedjar [17], who first proposed the introduction of a *micro-inertia* term due to damage evolution, and can on the other hand be compared to the micromorphic approach [15] for it involves an auxiliary nondissipative damage variable $\widetilde{\mathcal{D}}$. The latter is supposed to "bear" every nonlocal effects and is therefore involved in micro-inertia and the gradient terms of the crack surface density function.

The global kinetic and free energy of a solid occupying the domain Ω are thus:

$$K = \int_\Omega \left(\frac{1}{2}\rho\left\|\boldsymbol{v}\right\|^2 + \frac{1}{2}\beta\frac{\partial\widetilde{\mathcal{D}}}{\partial t}^2\right) dV \tag{13}$$

$$F = \int_\Omega \Psi(\boldsymbol{\varepsilon}, \mathcal{D}, \widetilde{\mathcal{D}}, \boldsymbol{\nabla}\widetilde{\mathcal{D}}) dV \tag{14}$$

in which ρ is the mass density of the solid, $\boldsymbol{v}$ is the velocity field, and β is the micro-inertia parameter. Though not written explicitly in the above energies,

both damage variables $\mathcal{D}$ and $\widetilde{\mathcal{D}}$ are forced to remain close to each other by means of a penalty function contained in the free energy density

$$g(\mathcal{D}, \widetilde{\mathcal{D}}) = \frac{\lambda}{2}\left(\widetilde{\mathcal{D}} - \mathcal{D}\right)^2, \quad \lambda \gg 1 \tag{15}$$

In addition to those energies, the work of external forces is as follows:

$$\mathcal{W}_e = \int_\Omega \boldsymbol{b} \cdot \boldsymbol{u} dV + \int_{\partial\Omega} \boldsymbol{T}_d \cdot \boldsymbol{u} dS \tag{16}$$

The above functions allows defining the Lagrangian functional $\mathcal{L} = K + \mathcal{W}_e - F$.

3.2 Exponential-based form of the free energy

In order to override the constraint $\mathcal{D} \leq 1$, we propose the following change of variable:

$$\mathcal{D} = 1 - e^{-q\mathscr{D}}, \quad q > 0, \tag{17}$$

where a new *relaxed damage variable* $\mathscr{D} \geq 0$ has been introduced. With such a variable, and using the notation $f(\mathcal{D}) = \hat{f}(\mathscr{D})$ for every damage-dependent function, the free energy density becomes in the extended Lagrangian context:

$$\hat{\Psi}(\boldsymbol{\varepsilon}, \mathscr{D}, \widetilde{\mathcal{D}}, \boldsymbol{\nabla}\widetilde{\mathcal{D}}) = \hat{\psi}^e(\boldsymbol{\varepsilon}, \mathscr{D}) + G_c \hat{\gamma}_{\ell_0}(\mathscr{D}, \boldsymbol{\nabla}\widetilde{\mathcal{D}}) + \hat{g}(\mathscr{D}, \widetilde{\mathcal{D}}) \tag{18}$$

In (18) the definitions of the crack surface density, degradation, and penalty functions are respectively:

$$\hat{A}(\mathscr{D}) = e^{-qn\mathscr{D}} \qquad q > 0,\ n \geq 1 \tag{19}$$

$$\hat{\gamma}_{\ell_0}(\mathscr{D}, \boldsymbol{\nabla}\widetilde{\mathcal{D}}) = \frac{1}{4\ell_0 c_w}\left(\left[1 - e^{-q\mathscr{D}}\right]^p + \ell_0^2 \left\|\boldsymbol{\nabla}\widetilde{\mathcal{D}}\right\|^2\right) \qquad p > 1 \tag{20}$$

$$\hat{g}(\mathscr{D}, \widetilde{\mathcal{D}}) = \frac{\lambda}{2}\left(\widetilde{\mathcal{D}} - (1 - e^{-q\mathscr{D}})\right)^2 \qquad \lambda \gg 1 \tag{21}$$

Notice that though the idea of a damage parameter belonging to $\mathbb{R}^+$ was already suggested by Pham and Marigo [43,44], it is to the authors knowledge the first time that such a variable is truly considered for its computational aspect. It is moreover worth insisting on the fact that, in contrast with the exponential-based model presented in [27] (see equation (22) in the reference), the free energy is not modified by the change of variable (*i.e* $\Psi \equiv \hat{\Psi}$).

3.3 Hamilton's variational principle

Based on the new expression of the free energy (18), the stationnarity of the action integral $\mathcal{A} = \int_{\mathcal{T}} \mathcal{L} dt$ is sought over some time interval $\mathcal{T} = [t_1, t_2]$ and considering vanishing variations on $\partial\mathcal{T}$. In addition, taking into account the relation between the infinitesimal strain tensor and the displacement vector:

$$\boldsymbol{\varepsilon} = \frac{1}{2}\left(\boldsymbol{\nabla} \boldsymbol{u} + \boldsymbol{\nabla}^T \boldsymbol{u}\right), \tag{22}$$

the following equation is derived:

$$\begin{aligned}\delta\mathcal{A} = \int_{\mathcal{T}}\int_{\Omega} \left\{ \left[-\rho \frac{\partial \boldsymbol{v}}{\partial t} + div\left(\frac{\partial \hat{\Psi}}{\partial \boldsymbol{\varepsilon}}\right) + \boldsymbol{b} \right] \cdot \delta \boldsymbol{u} + \left[-\beta \ddot{\widetilde{\mathcal{D}}} + div\left(\frac{\partial \hat{\Psi}}{\partial \boldsymbol{\nabla}\widetilde{\mathcal{D}}}\right) - \frac{\partial \hat{\Psi}}{\partial \widetilde{\mathcal{D}}} \right] \delta\widetilde{\mathcal{D}} - \frac{\partial \hat{\Psi}}{\partial \mathscr{D}} \delta\mathscr{D} \right\} d\Omega dt \\ + \int_{\mathcal{T}}\int_{\partial\Omega} \left\{ \left[-\frac{\partial \hat{\Psi}}{\partial \boldsymbol{\varepsilon}} \cdot \boldsymbol{n} + \boldsymbol{T}_d \right] \cdot \delta \boldsymbol{u} + \left[\frac{\partial \hat{\Psi}}{\partial \boldsymbol{\nabla}\widetilde{\mathcal{D}}} \cdot \boldsymbol{n} \right] \delta\widetilde{\mathcal{D}} \right\} ds dt = 0 \quad \forall \delta\boldsymbol{u}, \delta\mathscr{D}, \delta\widetilde{\mathcal{D}}\end{aligned} \tag{23}$$

The arbitrariness of variations $\delta\boldsymbol{u}, \delta\mathscr{D}, \delta\widetilde{\mathcal{D}}$ yields a set of three volume equations:

$$\left| \begin{aligned} &\rho \frac{\partial \boldsymbol{v}}{\partial t} - div\left(\frac{\partial \hat{\Psi}}{\partial \boldsymbol{\varepsilon}}\right) = \boldsymbol{b} \\ &-\frac{\partial \hat{\Psi}}{\partial \mathscr{D}} = 0 \\ &\beta \ddot{\widetilde{\mathcal{D}}} - div\left(\frac{\partial \hat{\Psi}}{\partial \boldsymbol{\nabla}\widetilde{\mathcal{D}}}\right) + \frac{\partial \hat{g}}{\partial \widetilde{\mathcal{D}}} = 0 \end{aligned} \right. \qquad \forall \boldsymbol{x} \in \Omega, \tag{24}$$

and two natural boundary conditions:

$$\left| \begin{aligned} &\frac{\partial \hat{\Psi}}{\partial \boldsymbol{\varepsilon}} \cdot \boldsymbol{n} = \boldsymbol{T}_d \\ &\frac{\partial \hat{\Psi}}{\partial \boldsymbol{\nabla}\widetilde{\mathcal{D}}} \cdot \boldsymbol{n} = 0 \end{aligned} \right. \qquad \forall \boldsymbol{x} \in \partial\Omega \tag{25}$$

In the above equations, the partial derivatives of the free energy density with respect to $\boldsymbol{\varepsilon}$ and $\mathscr{D}$ are respectively related to the Cauchy stress tensor $\boldsymbol{\sigma}$ and the thermodynamic force conjugate to the relaxed damage variable $\mathsf{Y}_{\mathscr{D}}$ *in the extended Lagrangian context*, namely:

$$\boldsymbol{\sigma} = \frac{\partial \hat{\Psi}}{\partial \boldsymbol{\varepsilon}} \tag{26}$$

$$\mathsf{Y}_{\mathscr{D}} = -\frac{\partial \hat{\Psi}}{\partial \mathscr{D}} \tag{27}$$

Indeed, with the nonlocal term carried by the auxiliary variable, the variational derivative in equation (2) reduces to a partial derivative.

At last, we consider the geometrical conservation law [46] with a non-conventional but intrinsic form based on the tensor product operator $\boxtimes$ introduced in [47]:

$$\frac{\partial \boldsymbol{\varepsilon}}{\partial t} = div\left(\frac{\boldsymbol{v}\otimes\boldsymbol{I}+\boldsymbol{I}\boxtimes\boldsymbol{v}}{2}\right) \qquad \text{with} \begin{cases} (\boldsymbol{v}\otimes\boldsymbol{I})_{ijk} = v_i\delta_{jk} \\ (\boldsymbol{I}\boxtimes\boldsymbol{v})_{ijk} = \delta_{ik}v_j \end{cases}, \tag{28}$$

as well as the change of variable:

$$\alpha = \frac{\partial\widetilde{\mathcal{D}}}{\partial t} \quad ; \quad \frac{\partial\hat{\Psi}}{\partial\boldsymbol{\nabla}\widetilde{\mathcal{D}}} = \frac{G_c\ell_0}{2c_w}\boldsymbol{\nabla}\widetilde{\mathcal{D}} = \frac{G_c\ell_0}{2c_w}\boldsymbol{h} \quad \text{and} \quad \frac{\partial\boldsymbol{h}}{\partial t} = div\,(\alpha\boldsymbol{I})\,, \tag{29}$$

in such a way that the first-order system of equations with source term, whose hyperbolicity will be shown in section 4, is written as:

$$\left|\begin{array}{l} \dfrac{\partial\boldsymbol{\varepsilon}}{\partial t} - div\left(\dfrac{\boldsymbol{v}\otimes\boldsymbol{I}+\boldsymbol{I}\boxtimes\boldsymbol{v}}{2}\right) = \boldsymbol{0} \\ \rho\dfrac{\partial\boldsymbol{v}}{\partial t} - div\,\boldsymbol{\sigma} = \boldsymbol{b} \\ \mathsf{Y}_{\mathscr{D}} = 0 \\ \dfrac{\partial\widetilde{\mathcal{D}}}{\partial t} = \alpha \\ \beta\dfrac{\partial\alpha}{\partial t} - \dfrac{G_c\ell_0}{2c_w}div\,\boldsymbol{h} = -\dfrac{\partial\hat{g}}{\partial\widetilde{\mathcal{D}}} \\ \dfrac{\partial\boldsymbol{h}}{\partial t} - div\,(\alpha\boldsymbol{I}) = \boldsymbol{0} \end{array}\right. \qquad \forall\boldsymbol{x}\in\Omega \tag{30}$$

3.4 Evolution equation for damage

Analogously to the normality rule for the bounded damage variable (12), the evolution of the relaxed damage variable is derived from the dual dissipation pseudo-potential $\hat{\varphi}^*(\mathsf{Y}_{\mathscr{D}})$ according to:

$$\frac{\partial\mathscr{D}}{\partial t} = \frac{\partial\hat{\varphi}^*(\mathsf{Y}_{\mathscr{D}})}{\partial\mathsf{Y}_{\mathscr{D}}} \tag{31}$$

Considering a Perzyna-type viscous damage evolution, the dual dissipation pseudo-potential is then taken under the following form:

$$\hat{\varphi}^*(\mathsf{Y}_{\mathscr{D}}) = \frac{1}{K+1}\frac{\langle f_{\mathscr{D}}(\mathsf{Y}_{\mathscr{D}})\rangle^{K+1}}{\eta_{\mathscr{D}}}, \qquad K\geq 1, \tag{32}$$

where $f_{\mathscr{D}}(\mathsf{Y}_{\mathscr{D}})$ is the yield surface, $\langle\bullet\rangle$ is the positive part operator, $\eta_{\mathscr{D}}$ is the damage viscosity and the exponent K is set to unity for simplicity in this work. This choice of the dissipation potential yields the damage evolution equation:

$$\frac{\partial\mathscr{D}}{\partial t} = \frac{\langle f_{\mathscr{D}}(\mathsf{Y}_{\mathscr{D}})\rangle}{\eta_{\mathscr{D}}}\frac{\partial f_{\mathscr{D}}(\mathsf{Y}_{\mathscr{D}})}{\partial\mathsf{Y}_{\mathscr{D}}}, \tag{33}$$

which replaces the third equation of system (30) in order to take into account irreversibility. For simplicity, the yield function is assumed to be equal to the thermodynamic force, that is:

$$f_{\mathscr{D}} = \mathsf{Y}_{\mathscr{D}} = -\frac{\partial \hat{\Psi}}{\partial \mathscr{D}} = -\frac{\partial \hat{\psi}^e}{\partial \mathscr{D}}(\boldsymbol{\varepsilon}, \mathscr{D}) - G_c \frac{\partial \hat{\gamma}_{\ell_0}}{\partial \mathscr{D}}(\mathscr{D}, \boldsymbol{\nabla}\widetilde{\mathcal{D}}) - \frac{\partial \hat{g}}{\partial \mathscr{D}}(\mathscr{D}, \widetilde{\mathcal{D}}), \tag{34}$$

leading to an irreversible non-dissipative model [14]. Dissipation can however be considered in various ways, for instance through the introduction of a non-zero threshold in $f_{\mathscr{D}}$ (see [14]).

Introducing the array vectors:

$$\boldsymbol{\mathcal{U}} = \begin{Bmatrix} \boldsymbol{\varepsilon} \\ \rho \boldsymbol{v} \\ \mathscr{D} \\ \widetilde{\mathcal{D}} \\ \beta\alpha \\ \boldsymbol{h} \end{Bmatrix} \quad ; \quad \boldsymbol{\mathcal{F}} = -\begin{Bmatrix} \frac{\boldsymbol{v}\otimes\boldsymbol{I}+\boldsymbol{I}\boxtimes\boldsymbol{v}}{2} \\ \boldsymbol{\sigma} \\ 0 \\ 0 \\ \frac{G_c \ell_0}{2c_w}\boldsymbol{h} \\ \alpha \boldsymbol{I} \end{Bmatrix} \quad ; \quad \boldsymbol{\mathcal{S}} = \begin{Bmatrix} \boldsymbol{0} \\ \boldsymbol{b} \\ \frac{\langle f_{\mathscr{D}}(\mathsf{Y}_{\mathscr{D}})\rangle}{\eta_{\mathscr{D}}} \\ \alpha \\ -\frac{\partial \hat{g}}{\partial \widetilde{\mathcal{D}}} \\ \boldsymbol{0} \end{Bmatrix}, \tag{35}$$

the governing system reads in compact form:

$$\frac{\partial \boldsymbol{\mathcal{U}}}{\partial t} + div\, \boldsymbol{\mathcal{F}} = \boldsymbol{\mathcal{S}}. \tag{36}$$

4 The Riemann problem and hyperbolicity

First note that the homogeneous part of system (36) does not involve damage nor auxiliary variable evolutions since the flux term in the third and fourth equations are zero. We can then momentarily restrict our attention to reduced versions of $\boldsymbol{\mathcal{U}}$ and $\boldsymbol{\mathcal{F}}$ in which the third and fourth terms are removed and denoted as $\overline{\boldsymbol{\mathcal{U}}}$ and $\overline{\boldsymbol{\mathcal{F}}}$ respectively. One-dimensional Riemann problems in direction $\boldsymbol{n}$ can be defined with those quantities:

$$\frac{\partial \overline{\boldsymbol{\mathcal{U}}}}{\partial t} + \frac{\partial \overline{\boldsymbol{\mathcal{F}}}_n}{\partial x_n} = \boldsymbol{0} \quad \text{with} \quad \begin{cases} \overline{\boldsymbol{\mathcal{U}}}(x_n, t=0) = \overline{\boldsymbol{\mathcal{U}}}_L \;\; if \;\; x_n < 0 \\ \overline{\boldsymbol{\mathcal{U}}}(x_n, t=0) = \overline{\boldsymbol{\mathcal{U}}}_R \;\; if \;\; x_n > 0 \end{cases} \tag{37}$$

where $x_n = \boldsymbol{x}\cdot\boldsymbol{n}$ and $\overline{\boldsymbol{\mathcal{F}}}_n = \overline{\boldsymbol{\mathcal{F}}}\cdot\boldsymbol{n}$ are projections along $\boldsymbol{n}$. The above problem is hyperbolic if the Jacobian matrix $\mathbf{J} = \partial\overline{\boldsymbol{\mathcal{F}}}_n/\partial\overline{\boldsymbol{\mathcal{U}}}$ has real eigenvalues and a set of independent eigenvectors. With the constitutive relations given in section 2, and the elasticity tensor $\mathbb{C}(\mathcal{D})$ being now a function of the relaxed damage variable $\hat{\mathbb{C}}(\mathscr{D})$, the Jacobian matrix reads:

$$\mathbf{J} = -\begin{bmatrix} \boldsymbol{0}^4 & \frac{\boldsymbol{I}\boxtimes\boldsymbol{n}+\boldsymbol{n}\otimes\boldsymbol{I}}{2\rho} & \boldsymbol{0}^2 & \boldsymbol{0}^3 \\ \hat{\mathbb{C}}^{\pm}\cdot\boldsymbol{n} & \boldsymbol{0}^2 & \boldsymbol{0}^1 & \boldsymbol{0}^2 \\ \boldsymbol{0}^2 & \boldsymbol{0}^1 & 0 & \frac{G_c\ell_0}{2c_w}\boldsymbol{n} \\ \boldsymbol{0}^3 & \boldsymbol{0}^2 & \frac{\boldsymbol{n}}{\beta} & \boldsymbol{0}^2 \end{bmatrix} \tag{38}$$

in which $\mathbf{0}^k$ is a kth order zero tensor. The block-diagonal structure of the Jacobian first shows that two Riemann problems can be solved in an uncoupled manner: one associated to strain and linear momentum and one associated to the derivatives of the auxiliary variable $\beta\alpha$ and $\boldsymbol{h}$. Second, the characteristic structure of the uncoupled problem is given by the characteristic structure of the two sub-problems, namely, one has for non-zero eigenvalues:

$$-\begin{bmatrix} \mathbf{0}^4 & \frac{\boldsymbol{I}\boxtimes\boldsymbol{n}+\boldsymbol{n}\otimes\boldsymbol{I}}{2\rho} \\ \hat{\mathbb{C}}^{\pm}\cdot\boldsymbol{n} & \mathbf{0}^2 \end{bmatrix} \begin{Bmatrix} \boldsymbol{\varepsilon}^I \\ \rho\boldsymbol{v}^I \end{Bmatrix} = c_I^e \begin{Bmatrix} \boldsymbol{\varepsilon}^I \\ \rho\boldsymbol{v}^I \end{Bmatrix} = c_I^e \boldsymbol{\mathcal{R}}_I^e \tag{39}$$

$$-\begin{bmatrix} 0 & \frac{G_c\ell_0}{2c_w}\boldsymbol{n} \\ \frac{\boldsymbol{n}}{\beta} & \mathbf{0}^2 \end{bmatrix} \begin{Bmatrix} \beta\alpha^I \\ \boldsymbol{h}^I \end{Bmatrix} = c_I^d \begin{Bmatrix} \beta\alpha^I \\ \boldsymbol{h}^I \end{Bmatrix} = c_I^d \boldsymbol{\mathcal{R}}_I^d, \tag{40}$$

where $c_I^{e,d}$ denote characteristic speeds, $\boldsymbol{\mathcal{R}}_I^{e,d}$ are right eigenvectors and the superscripts "e" and "d" stand for the elastic and damage part of the system respectively.

4.1 Elastic part

Expanding the first eigensystem, one writes:

$$-\frac{\boldsymbol{v}^I\otimes\boldsymbol{n}+\boldsymbol{n}\otimes\boldsymbol{v}^I}{2} = c_I^e\boldsymbol{\varepsilon}^I \tag{41}$$

$$-\left(\hat{\mathbb{C}}^{\pm}\cdot\boldsymbol{n}\right):\boldsymbol{\varepsilon}^I = \rho c_I^e\boldsymbol{v}^I \tag{42}$$

Substituting the first equation into the second one and taking into account the symmetries of the elasticity tensor, we get:

$$-\left(\boldsymbol{n}\cdot\hat{\mathbb{C}}^{\pm}\cdot\boldsymbol{n}\right)\cdot\boldsymbol{v}^I = \rho {c_I^e}^2\boldsymbol{v}^I, \tag{43}$$

which corresponds to the eigensystem of the (symmetric) second-order acoustic tensor $\boldsymbol{\Gamma}^{\pm} = \boldsymbol{n}\cdot\hat{\mathbb{C}}^{\pm}\cdot\boldsymbol{n}$. For a problem in N space dimensions, the acoustic tensor admit N – not necessarily distinct – positive eigenvalues ω_k that provide $2N$ non-zero characteristic speeds $c_{I(k)} = \pm\sqrt{\frac{\omega_k}{\rho}}$. With the form of the energy density considered in equation (10), the acoustic tensor reads:

$$\boldsymbol{\Gamma}^{+} = \mu\hat{A}(\mathscr{D})\left(\boldsymbol{I}+\frac{1}{3}\boldsymbol{n}\otimes\boldsymbol{n}\right)+\kappa\hat{A}(\mathscr{D})\boldsymbol{n}\otimes\boldsymbol{n} \tag{44}$$

$$\boldsymbol{\Gamma}^{-} = \mu\hat{A}(\mathscr{D})\left(\boldsymbol{I}+\frac{1}{3}\boldsymbol{n}\otimes\boldsymbol{n}\right)+\kappa\boldsymbol{n}\otimes\boldsymbol{n} \tag{45}$$

Denoting the eigenvectors of the acoustic tensor $\boldsymbol{r}^k$ and using $\pm$ superscripts on the eigenvalues as well, the following eigensystems are written:

$$\boldsymbol{\Gamma}^{+}\cdot\boldsymbol{r}^k = \mu\hat{A}(\mathscr{D})\boldsymbol{r}^k+\hat{A}(\mathscr{D})\left(\frac{1}{3}\mu+\kappa\right)\boldsymbol{n}(\boldsymbol{r}^k\cdot n) = \omega_k^{+}\boldsymbol{r}^k \tag{46}$$

$$\boldsymbol{\Gamma}^{-}\cdot\boldsymbol{r}^k = \mu\hat{A}(\mathscr{D})\boldsymbol{r}^k+\left(\hat{A}(\mathscr{D})\frac{1}{3}\mu+\kappa\right)\boldsymbol{n}(\boldsymbol{r}^k\cdot n) = \omega_k^{-}\boldsymbol{r}^k \tag{47}$$

It is seen from the above equations that the eigenvectors are in any case either colinear or perpendicular to the direction $\boldsymbol{n}$. The associated eigenvalues giving the characteristic speeds of *longitudinal* and *shear* waves respectively:

$$\boldsymbol{r}^k = \boldsymbol{n} \Rightarrow \begin{cases} \omega_k^+ = \left(\dfrac{4}{3}\mu + \kappa\right) \hat{A}(\mathscr{D}) \quad \text{and } c^e_{I(k)} = \pm\sqrt{\dfrac{\left(\frac{4}{3}\mu + \kappa\right) \hat{A}(\mathscr{D})}{\rho}} & \text{if tr } \boldsymbol{\varepsilon} \geq 0 \\ \omega_k^- = \dfrac{4}{3}\mu\hat{A}(\mathscr{D}) + \kappa \quad \text{and } c^e_{I(k)} = \pm\sqrt{\dfrac{\frac{4}{3}\mu\hat{A}(\mathscr{D}) + \kappa}{\rho}} & \text{if tr } \boldsymbol{\varepsilon} < 0 \end{cases} \tag{48}$$

$$\boldsymbol{r}^k \perp \boldsymbol{n} \Rightarrow \omega_k^{\pm} = \mu\hat{A}(\mathscr{D}) \quad \text{and } c^e_{I(k)} = \pm\sqrt{\frac{\mu\hat{A}(\mathscr{D})}{\rho}} \quad \forall \text{ tr } \boldsymbol{\varepsilon} \tag{49}$$

Since, $\hat{A}(\mathscr{D}) \in [0, 1[$ and $\kappa, \mu > 0$, the eigenvalues of the acoustic tensor are obviously positive. The characteristic speeds are therefore real. The corresponding linearly independent right eigenvectors are:

$$\boldsymbol{\mathcal{R}}^e_{I(k)} = \left\{ \begin{array}{c} -\frac{\boldsymbol{r}^k \otimes \boldsymbol{n} + \boldsymbol{n} \otimes \boldsymbol{r}^k}{2} \\ \rho c^e_{I(k)} \boldsymbol{r}^k \end{array} \right\} \tag{50}$$

At last, the linearly independent eigenvectors associated with the zero characteristic speed of multiplicity N are:

$$\boldsymbol{\mathcal{R}}^e_0 = \left\{ \begin{array}{c} \boldsymbol{\varepsilon}^0 \\ \boldsymbol{0} \end{array} \right\}, \tag{51}$$

with $\boldsymbol{\varepsilon}^0$ non-trivial solutions of the homogeneous underdetermined system $\left(\hat{\mathbb{C}}^{\pm} \cdot \boldsymbol{n}\right) : \boldsymbol{\varepsilon}^0 = \boldsymbol{0}$.

4.2 Damage part

Let us now focus on the second part of the eigensystem given by equation (40):

$$-\frac{G_c \ell_0}{2c_w} \boldsymbol{n} \cdot \boldsymbol{h}^I = c_I^d \beta \alpha^I \tag{52}$$

$$-\boldsymbol{n}\alpha^I = c_I^d \boldsymbol{h}^I \tag{53}$$

Two non-zero characteristic fields are first derived by projecting the second equation on $\boldsymbol{n}$ and plugging it into the first one:

$$\frac{G_c \ell_0}{2c_w} \alpha^I = {c_I^d}^2 \beta \alpha^I \tag{54}$$

$$\boldsymbol{h}^I = -\frac{\alpha^I}{c_I^d} \boldsymbol{n} \tag{55}$$

It thus comes the characteristic speeds and associated independent eigenvectors:

$$c_I^d = \pm\sqrt{\frac{G_c\ell_0}{2c_w\beta}} = \pm c_{\mathcal{D}} \qquad ; \qquad \boldsymbol{\mathcal{R}}_I^d = \left\{ \begin{array}{c} \beta c_I^d \\ -\boldsymbol{n} \end{array} \right\} \tag{56}$$

The independent eigenvectors associated with the zero-eigenvalue of multiplicity $N-1$ are found by taking $\alpha^I = 0$ and $\boldsymbol{h}^I$ perpendicular to $\boldsymbol{n}$.

4.3 Summary of the results

It has been shown in this section that the elastic problem may involve pressure and shear waves whose damage-dependent real speeds respectively read:

$$c_p(\mathscr{D}) = \left\{ \begin{array}{ll} \pm\sqrt{\dfrac{\left(\frac{4}{3}\mu+\kappa\right)\hat{A}(\mathscr{D})}{\rho}} & \text{if tr } \boldsymbol{\varepsilon} \geq 0 \\ \pm\sqrt{\dfrac{\frac{4}{3}\mu\hat{A}(\mathscr{D})+\kappa}{\rho}} & \text{if tr } \boldsymbol{\varepsilon} < 0 \end{array} \right. \tag{57}$$

$$c_s(\mathscr{D}) = \pm\sqrt{\frac{\mu\hat{A}(\mathscr{D})}{\rho}} \quad \forall \text{ tr } \boldsymbol{\varepsilon} \tag{58}$$

In addition, the associated eigenvectors of the Jacobian are linearly independent.

Analogously, the damage problem implies the propagation of leftward and rightward waves of real speeds:

$$c_{\mathcal{D}} = \pm\sqrt{\frac{G_c\ell_0}{2c_w\beta}} \tag{59}$$

and is characterized by a complete set of independent eigenvectors.

Hyperbolicity of the system is therefore unconditionally ensured for this model. Notice that other decompositions exist, such that for instance spectral decompositions considered by Miehe and coworkers [35] or Borden and coworkers [5], for which hyperbolicity is nevertheless still to be proved.

The expression of wave speeds associated with the damage problem involve the micro-inertia parameter β and does therefore require further investigations supported with experimental works in order to be physically relevant. In the meantime, the micro-inertia is tuned in order to obtain a given ratio between pressure and damage wave speeds in the undamaged medium, namely:

$$\frac{c_p^2(\mathcal{D}=0)}{c_{\mathcal{D}}^2} = \frac{2c_w\beta\left(\frac{4}{3}\mu+\kappa\right)}{\rho G_c\ell_0} = K_\beta \geq 1 \quad \Rightarrow \quad \beta = K_\beta\frac{\rho G_c\ell_0}{2c_w\left(\frac{4}{3}\mu+\kappa\right)} \tag{60}$$

In what follows, K_β is referred to as the *micro-inertia factor*.

5 Finite Volume solution

The numerical procedure used to solve the non-homogeneous system (36) has been presented in [14] for one-dimensional problems. It consists in discretizing in time the system using the explicit forward Euler method and solving separately at each time step the homogeneous part and the source term using a fractional-step method [29]. In this work as in the prior, Godunov's splitting in which the source term part is solved implicitly by means of the backward Euler method is employed, and a first-order finite volume scheme is used to solve the homogeneous part for one-dimensional problems.

For the two-dimensional problems considered in this paper, however, higher-order as well as transverse flux terms allowing a significant improvement of the numerical solution are used and presented in the following. Moreover, the Riemann solvers used for the elastic and the damage parts are briefly presented. Notice that the numerical solution is not restricted to one and two-dimensional problems and can be extended to three-dimensional ones providing some implementation efforts.

5.1 The flux-difference splitting method

Consider the partition of the solid domain Ω under consideration based on N_c non-overlapping unstructured quadrilateral cells $\Omega = \bigcup_{i=1}^{N_c} \Omega_i$. The cell-centered approximation $\boldsymbol{U}_i$ of the vector of conserved quantities $\boldsymbol{\mathfrak{U}}$ can be constructed in each finite volume by integral averaging. Integration of the system of conservation laws associated with (36) (*i.e.* setting $\boldsymbol{\mathfrak{S}} = \boldsymbol{0}$) over a grid cell i leads to the following system of ordinary differential equation:

$$\frac{d\boldsymbol{U}_i}{dt} = -\frac{1}{\mathsf{A}_i} \sum_{p=1}^{4} L_p \boldsymbol{F}_p, \tag{61}$$

where A_i is the area of cell i, and $\boldsymbol{F}_p$ is the numerical flux computed at edge p of length L_p. In the flux-difference splitting version of finite volumes [29], it reduces to the computation of *fluctuation terms* $\mathcal{A}^{\pm}(\Delta \boldsymbol{U}_p)$ according to:

$$\sum_{p=1}^{4} L_p \boldsymbol{F}_p = \sum_{i=1}^{P} L_i \mathcal{A}^{+}(\Delta \boldsymbol{U}_i) + \sum_{i=1}^{Q} L_i \mathcal{A}^{-}(\Delta \boldsymbol{U}_i), \tag{62}$$

where P is the set of edges having an inward unit normal and Q the set of edges having an outward unit normal ($P+Q=4$) as depicted in figure 1. Moreover, $\Delta \boldsymbol{U}_k = \boldsymbol{U}_D - \boldsymbol{U}_U$ is the jump between the known states in downstream (D) and upstream (U) adjacent cells of edge k according to the orientation of its normal. The ingoing (+) and outgoing (-) fluctuations at edge k are then

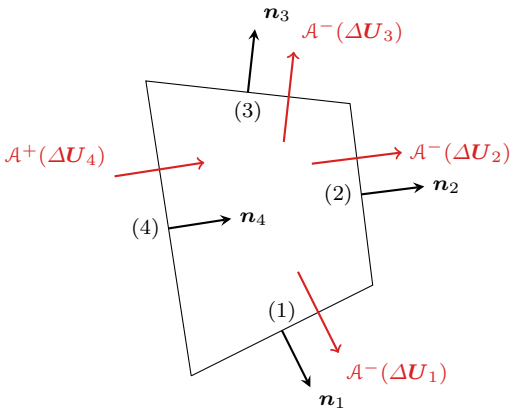


Figure 1: Non-cartesian quadrangular finite volume cell and normal fluctuations through cell edges (red arrows). The edge numbers are indicated in parentheses.

computed as:

$$\mathcal{A}^+(\Delta \boldsymbol{U}_k) = (\boldsymbol{F}(\boldsymbol{U}_U) - \boldsymbol{F}(\boldsymbol{U}^*)) \cdot \boldsymbol{n}_k \tag{63}$$

$$\mathcal{A}^-(\Delta \boldsymbol{U}_k) = (\boldsymbol{F}(\boldsymbol{U}^*) - \boldsymbol{F}(\boldsymbol{U}_D)) \cdot \boldsymbol{n}_k \tag{64}$$

where $\boldsymbol{U}^*$ denotes the stationary solution of the Riemann problem defined at edge k, whose computation is detailed below.

5.2 Riemann solvers

As highlighted in section 4, the Riemann problem defined between finite volume cells, with initial conditions $\boldsymbol{U}_U$ and $\boldsymbol{U}_D$, can be decoupled into elastic and damage parts, for which the following *reduced* array vectors are considered:

$$\overline{\boldsymbol{U}}^e = \left\{ \begin{matrix} \boldsymbol{\varepsilon} \\ \rho \boldsymbol{v} \end{matrix} \right\} \quad ; \quad \overline{\boldsymbol{U}}^d = \left\{ \begin{matrix} \beta \alpha \\ \boldsymbol{h} \end{matrix} \right\} \tag{65}$$

For the elastic part, the linear system resulting from the expansion of the initial data on the eigenbasis of dimension M_w^e [52], namely:

$$\Delta \boldsymbol{U}^e = \mathbf{R}^e \boldsymbol{\delta} = \sum_{k=1}^{M_w^e} \boldsymbol{\mathcal{R}}_k^e \delta_k = \sum_{k=1}^{M_w^e} \boldsymbol{\mathcal{W}}_k^e, \tag{66}$$

is first solved for the wave strength coefficients $\boldsymbol{\delta}$ and, in turn, the wave strengths $\boldsymbol{\mathcal{W}}^e$. The latter can be seen as the jump discontinuity carried by each wave. The fluctuations are then computed as [28]:

$$\mathcal{A}^+(\Delta \boldsymbol{U}^e) = \sum_{\substack{k \\ c_k^e > 0}} c_k^e \boldsymbol{\mathcal{W}}_k^e \quad ; \quad \mathcal{A}^-(\Delta \boldsymbol{U}^e) = \sum_{\substack{k \\ c_k^e < 0}} c_k^e \boldsymbol{\mathcal{W}}_k^e \tag{67}$$

In the above methodology, $\mathbf{R}$ is a matrix whose column k is the kth eigenvector of the Jacobian matrix associated with the wave speed c_k^e. It is worth noticing that as in [48], the speed and eigenvector are evaluated based on the damage value in the cell in which the associated wave propagates.

For the damage part, only two propagating waves separating three constant states are involved at cell interfaces. The HLL approximate Riemann solver [52] allows the direct evaluation of the stationary flux and hence, of the fluctuations:

$$\boldsymbol{F}(\boldsymbol{U}^{d,*}) = \frac{s_D \boldsymbol{F}(\boldsymbol{U}_U^d) - s_U \boldsymbol{F}(\boldsymbol{U}_D^d) + s_U s_D (\boldsymbol{U}_D^d - \boldsymbol{U}_U^d)}{s_D - s_U} \quad \Rightarrow \begin{cases} \mathcal{A}^+(\Delta \boldsymbol{U}^d) = s_D(\boldsymbol{U}_D^d - \boldsymbol{U}^{d,*}) \\ \mathcal{A}^-(\Delta \boldsymbol{U}^d) = s_U(\boldsymbol{U}^{d,*} - \boldsymbol{U}_U^d) \end{cases} \tag{68}$$

where $s_{D,U} = \pm c_{\mathcal{D}}$ as defined in equation (59).

5.3 High order fluxes

Though the flux-difference splitting scheme presented above is first-order accurate in space, its solutions can on the one hand be improved by considering total variation diminishing methods [28]. Indeed, second-order accuracy in space can be achieved by adding higher-order flux terms to the base fluctuations (62) computed at edge j:

$$\boldsymbol{F}_j^{HO} = \frac{1}{2} \sum_{i=1}^{M_w} |c_i| \left(1 - \frac{\Delta t}{\Delta s_j} |c_i|\right) \tilde{\boldsymbol{\mathcal{W}}}_i \tag{69}$$

where M_w is the number of waves involved in the problem (*i.e.* elastic or damage), s_j is the distance between the barycenters of cells sharing the edge j, and $\tilde{\boldsymbol{\mathcal{W}}}_i$ is the limited wave strength, computed as:

$$\tilde{\boldsymbol{\mathcal{W}}}_i = \phi\left(\frac{\boldsymbol{\mathcal{W}}_i^U \cdot \boldsymbol{\mathcal{W}}_i}{\|\boldsymbol{\mathcal{W}}_i\|^2}\right) \boldsymbol{\mathcal{W}}_i \tag{70}$$

in which $\boldsymbol{\mathcal{W}}_i^U$ is the corresponding wave strength *computed at the upwind edge* (*i.e.* the opposite edge with respect to the normal orientation) and ϕ is a limiting function [50]. In the present work, the function:

$$\phi(\theta) = \max\left(0, \min(1, 2\theta), \min(2, \theta)\right), \tag{71}$$

defining the Superbee limiter, is considered. Note that for unstructured grids, the wave strengths of the upwind edge in (70) are expressed in the local frame of edge i (see [22] for details).

On the other hand, transverse correction terms allowing to account for the influence of waves coming from cells sharing one nodes with the edge can be considered. Such corrections, known as the *Corner Transport Upwind method (CTU)* [9] enables significant improvements of accuracy and stability for problems in which quantities are modified by different waves, as for elasticity and

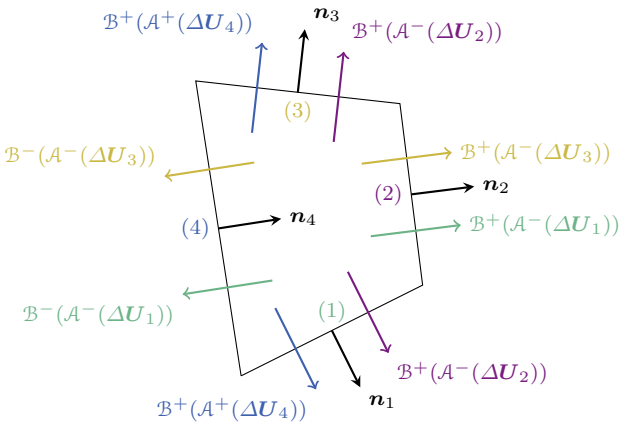


Figure 2: Non-cartesian quadrangular finite volume cell and transverse fluctuations through cell edges. The edge numbers are indicated in color in parentheses, the color being taken for the transverse fluctuations the edge gives rise to.

Poisson effect. They are thus only considered for the elastic problem in that work.

The normal fluctuations computed at edge k from the solution of the Riemann problem (67) modifies the interface flux of one of its adjacent edge, say edge i, due to wave propagation in the tangential direction. This is taken into account by first projecting the normal fluctuations onto the characteristic basis evaluated at edge i:

$$\mathcal{A}^{\pm}(\Delta \boldsymbol{U}_k^e) = \sum_{k=1}^{M_w} \boldsymbol{\mathcal{R}}_k^{e,i} \gamma_k = \mathbf{R}^{e,i} \boldsymbol{\gamma} \tag{72}$$

where, analogously to the normal problem, a linear system is solved for the coefficients $\boldsymbol{\gamma}$. Those coefficients allow the computation of transverse fluctuations *flowing through edge* i from edge k as:

$$\mathcal{B}^+(\mathcal{A}^{\pm}(\Delta \boldsymbol{U}_k^e)) = \sum_{\substack{j \\ c_j^e > 0}}^{M_w} c_j^e \boldsymbol{\mathcal{R}}_j^{e,i} \gamma_j \tag{73}$$

$$\mathcal{B}^-(\mathcal{A}^{\pm}(\Delta \boldsymbol{U}_k^e)) = \sum_{\substack{j \\ c_j^e < 0}}^{M_w} c_j^e \boldsymbol{\mathcal{R}}_j^{e,i} \gamma_j \tag{74}$$

in which the sign of the characteristic speed c_j^e, and therefore of the operator $\mathcal{B}$, is governed by the orientation of the normal to edge i. As illustrated in figure 2, the normal fluctuation computed at edge (4) has an influence on the interface flux of edges (1) and (3), both resulting from propagation in the directions $\boldsymbol{n}_1$

and $\boldsymbol{n}_3$, hence the $\mathcal{B}^+$ operator. Conversely, the normal fluctuation at edge (1) acts on edges (2) and (4) due to wave propagation in the direction $\boldsymbol{n}_2$ and opposite to $\boldsymbol{n}_4$, resulting in positive and negative transverse operators $\mathcal{B}^+$ and $\mathcal{B}^-$ respectively.

All the transverse fluctuations contribute to flux-difference splitting scheme through a transverse flux term computed at edge j:

$$\boldsymbol{F}_j^{Tran} = \frac{\Delta t}{2L_j}\left[\sum_{k=1}^{P_j}\mathcal{B}^{\pm}(\mathcal{A}^+(\Delta\boldsymbol{U}_k)) + \sum_{l=1}^{Q_j}\mathcal{B}^{\pm}(\mathcal{A}^-(\Delta\boldsymbol{U}_l))\right] \tag{75}$$

in which P_j and Q_j denote the set of edges adjacent to j and having respectively inward and outward unit normals.

Once all the contributions presented above gathered, the first-order explicit time discretization leads to the following conservative update in the cell i:

$$U_i^{n+1} = U_i^n - \underbrace{\frac{\Delta t}{\mathsf{A}_i}\left(\sum_{k=1}^{P} L_k\mathcal{A}^+(\Delta\boldsymbol{U}_k) + \sum_{l=1}^{Q} L_l\mathcal{A}^-(\Delta\boldsymbol{U}_l)\right)}_{\text{First-order}} - \underbrace{\frac{\Delta t}{\mathsf{A}_i}\left(\sum_{k=1}^{P}(\boldsymbol{F}_k^{HO}+\boldsymbol{F}_k^{Tran}) - \sum_{l=1}^{Q}(\boldsymbol{F}_l^{HO}+\boldsymbol{F}_l^{Tran})\right)}_{\text{High-order}} \tag{76}$$

As can be seen, higher-order and transverse fluxes are counted positively (*resp.* negatively) for edges having an inward (*resp.* outward) unit normal vector in cell i.

Remark 3 The time step Δt resulting from the (first-order) explicit time discretization of the continuum equations must be adapted during computations in order to satisfy the CFL condition

$$CFL = \max_j\{c_p(\mathscr{D}_j), c_{\mathcal{D}}\} \times \frac{\Delta t}{\min_i L_i} \leq 1 \tag{77}$$

where $\mathscr{D}_j$ and L_i are the damage value and the length of edge i in cell j. In the present work, Δt is set so that $CFL = 0.5$.

6 Numerical results

6.1 One-dimensional multifragmentation test

The exponential formulation of gradient damage models is first illustrated on a one-dimensional problem already considered in [14]. It consists in a one-dimensional domain with Dirichlet boundary conditions on the velocity on both ends and a linear initial velocity profile (see figure 3). This setting can be used to model the fragmentation of spherical or cylindrical thin shells undergoing expansion at constant strain rate.

The values of the material parameters kept constant in all the one-dimensional numerical simulations are given in table 1. Note that the characteristic length is only 10 times smaller than the domain length, in such a way that the number of cells contained in the damage length scale can easily be very high.

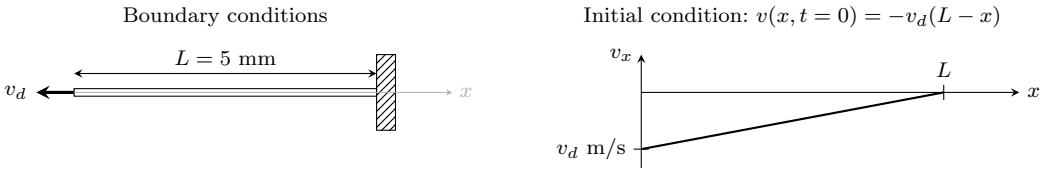


Figure 3: Geometry and loading of the multifragmentation test

E (GPa)	ρ (kg·m^{-3})	ℓ_0 (m)	$\eta_{\mathscr{D}}$ (Pa·s)	G_c (Pa)	λ (Pa)
27	2500	5×10^{-5}	1×10^{-4}	0.1	1×10^{6}

Table 1: Material parameters used for the multifragmentation test.

Influence of the exponential power q

We first propose to look at the solutions computed with both AT1 and AT2 models for several values of the parameter q and for an enforced velocity $v_d = -0.1$ m/s, which corresponds to an enforced strain rate $\dot{\varepsilon} = 20$ s^{-1}.

Figure 4 shows superpositions of final profiles of the damage variable $\mathcal{D} = 1 - e^{-q\mathscr{D}}$ computed with the considered values of q for AT models on a grid made of 4000 finite volume cells. It then appears that q plays an important role on the final solution computed. Indeed, the number and position of peaks as well as the lowest damage level obtained at the end of computations differ when q changes for both AT1 and AT2. However the influence of q on the number of cracks that is, the zones where $\mathcal{D} \approx 1$, and on the lower bound of damage seems to saturate as q increases, thus exhibiting some q-convergence of the proposed change of variable.

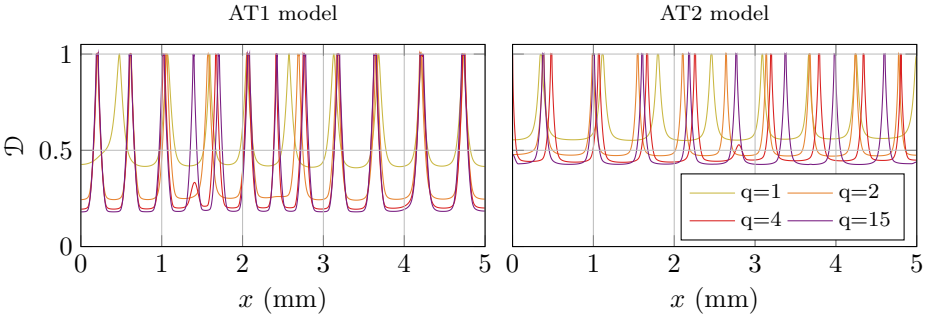


Figure 4: Final damage profile computed with finite volumes simulations of the multifragmentation test (4000 cells) using the exponential formulations of AT1 and AT2 models for several values of the parameter q.

The aforementioned q-convergence is confirmed by the results depicted in figure 5, in which the evolution with q of the surface damage energy function:

$$W^{\mathscr{D}} = \int_0^L \left[G_c \hat{\gamma}_{\ell_0}(\mathscr{D}, \boldsymbol{\nabla}\widetilde{\mathcal{D}}) + \hat{g}(\mathscr{D}, \widetilde{\mathcal{D}}) \right] dx, \tag{78}$$

is shown. As can be seen, the surface damage energy – which is dominated by

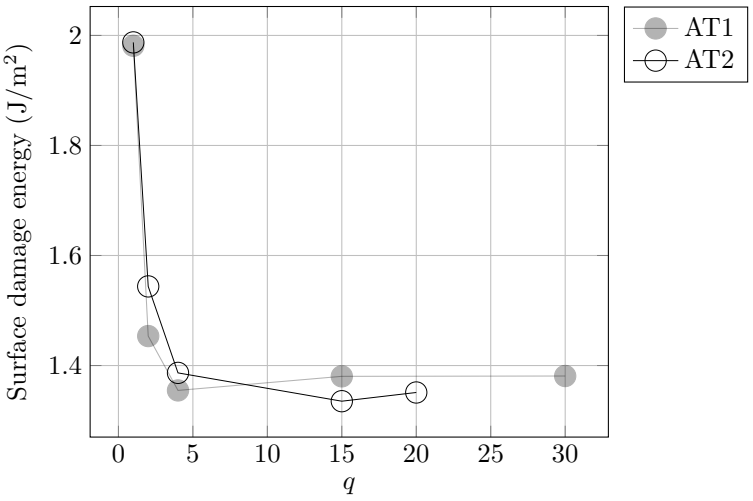


Figure 5: Final surface damage energy vs exponential parameter q

the local term of the crack surface density function and hence, by the integral of $\mathcal{D}$ – converges as q is increased regardless of the AT model considered. This is why only $q \leq 20$ has been considered for AT2 while $q = 30$ does not lead to a prohibitive computational time using AT1 model. It is nevertheless worth noticing that the computational cost drastically increases for $q \geq 10$ with AT2 model. This is shown in figure 6 in which the walltime normalized with respect to that of the shortest computation as well as the ratio between the cumulated time of Godunov's splitting steps with are plotted *versus* the value of q. Figure 6b shows that when some threshold is crossed, the implicit solution of the source term suddenly requires much more computational time. This is most likely due to the fact that the ODE system becomes very stiff for such values of q.

Mesh convergence

We now focus on the final values of the average fragment length and of the surface damage energy as mesh is refined. While the latter has already been defined above, the former is defined as the mean length of cells neighborhoods satisfying $\mathcal{D} \leq 0.98$, the situation $\mathcal{D} > 0.98$ being then considered as a fully

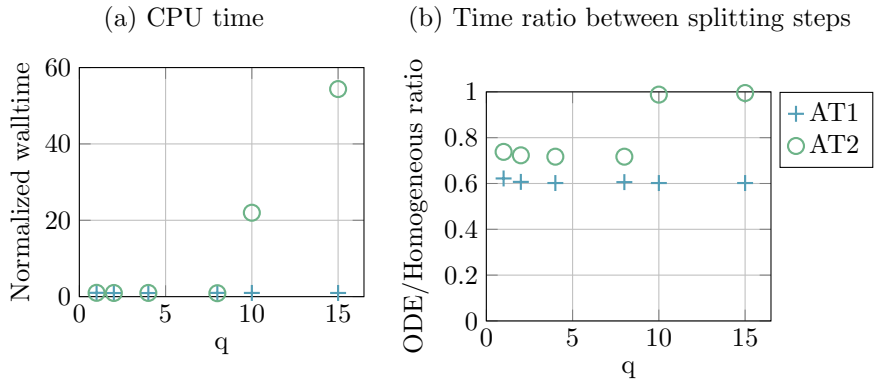


Figure 6: Effect of the value of the exponential coefficient q on the computational time

developed crack. The q-convergence identified previously allows to restrict the convergence analysis to the setting $q = 4$, beyond which the effect of q on the final damage energy seems to be very small as depicted in figure 5. Figure

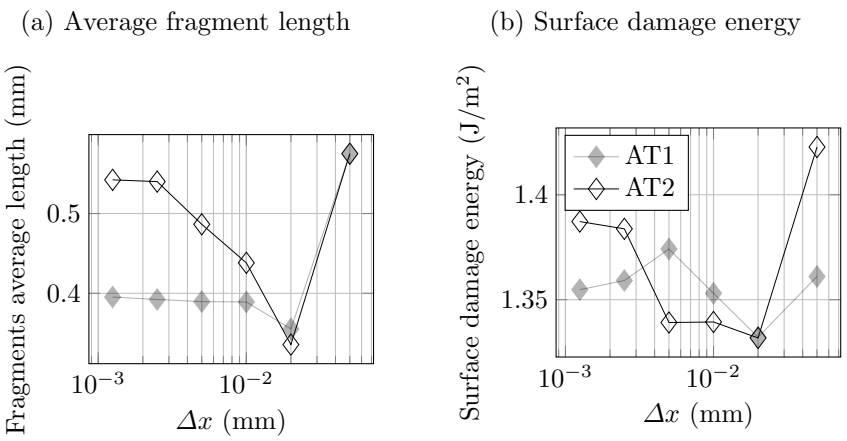


Figure 7: Mesh convergence curves in terms of average fragment lengths and surface damage energies for AT1 and AT2 models ($q = 4$). The legend stands for both subfigures.

7 first shows an obvious mesh convergence in terms of the average fragment length regardless of the AT model considered. In contrast, the energy curves do not really have nearly horizontal slopes for fine meshes. Nevertheless, the relative errors between the first and last values are 0.4% and 2% for AT1 and AT2 models respectively, which may indicate that the damage energy is accurately computed before convergence of the fragment length.

Effect of micro-inertia

We now focus on the effect micro-inertia by considering a mesh made of 1000 finite volume cells for the following values of the micro-inertia factor $K_\beta = \{1, 25, 100, 400\}$. Recall that, according to the definition of (60), damage waves speed is $\sqrt{K_\beta}$ times smaller than the speed of pressure waves *in the undamaged medium*. Figure 8 shows iso-values of the damage variable $\mathcal{D}$ in the $x-t$ plane that is, horizontal slices give the damage profile in the domain at different times for the AT1 model (considering the AT2 model leads to similar observations). It is seen that even though damage starts increasing exactly at the same time[1], its evolution is slower as micro-inertia increases, which results in a fragmentation triggering that is delayed. Next, micro-inertia may also

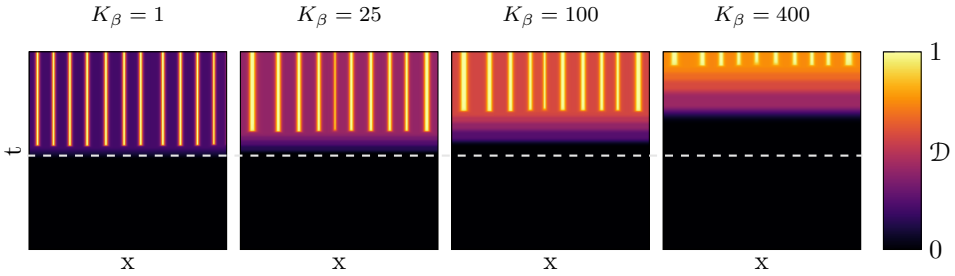


Figure 8: Damage variable $\mathcal{D}$ in the $x-t$ plane for different values of the micro-inertia factor K_β. AT1 model with $q = 4$ and 1000 finite volume cells.

influence the fragmentation pattern that is, the number and width of cracks. In addition to the lower damage level that becomes higher and higher as K_β increases, the final surface damage energy also increases with micro-inertia as shown in figure 9.

The crack thickness increase that has been mentioned can be explained by looking at the evolution of the field $\alpha = \tilde{\tilde{\mathcal{D}}}$. In order to compare quantities ranging in similar intervals regardless the value of the micro-inertia parameter, the following normalization is defined:

$$\overline{\alpha} = \frac{\alpha - \min_{t,x}(\alpha)}{\max_{t,x}(\alpha - \min_{t,x}(\alpha))} \in [0, 1]\,,$$

Then figure 10 shows isovalues in the $x-t$ plane of the normalized variable $\overline{\alpha}$ plotted for $K_\beta = 1$ and $K_\beta = 400$ from the time at which $\mathcal{D}$ starts varying to the end of the computation. In these plots, the zones where the maximum value $\overline{\alpha} = 1$ correspond to cracks.

[1] the delay that is observed between the starting times of damage evolution as K_β increases is only apparent and due to the fact that the rate of change of $\mathcal{D}$ is lower and lower and "spreads" the color map.

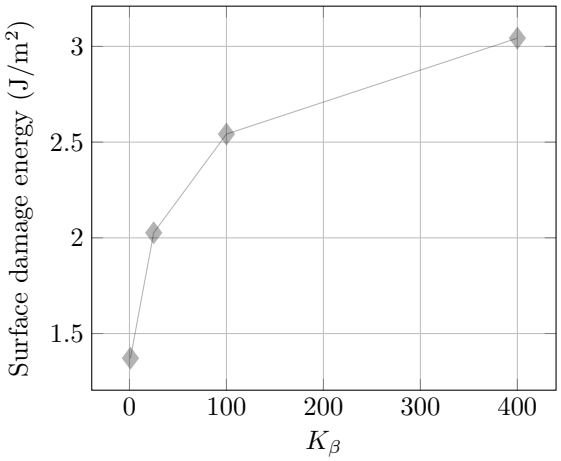


Figure 9: Evolution of the final surface damage energy with microinertia (1000 finite volume cells, AT1 model with $q = 4$)

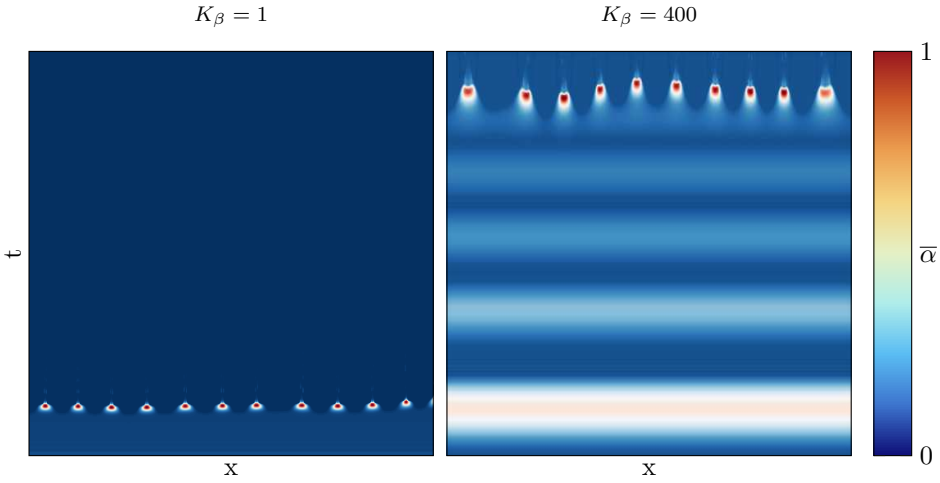


Figure 10: Isovalues of the normalized variable $\overline{\alpha}$ in the $x - t$ plane for two values of the micro-inertia factor K_β (both vertical axes have the same scale).

First, one can see that α has an oscillating nature, which is conferred by the source term part of the last equation of system (24):

$$\beta\ddot{\widetilde{\mathcal{D}}} = \lambda(\widetilde{\mathcal{D}} - \mathcal{D}),$$

whose homogeneous part admits harmonic solutions with angular frequency $\omega = \frac{\lambda}{\beta}$.

Next, figure 10 shows that the homogeneous evolution in space of α eventually stops owing to the propagation of *damage unloading waves*. Those waves separate regions in which $\overline{\alpha}$ either suddenly decreases or continues increasing and leave the "red triangle signature" that can be seen in the $x-t$ planes. If at some point, damage can reach a value sufficiently large before a damage unloading wave passes, a crack is formed. Since damage waves travel with speed $c_{\mathcal{D}}$, which decreases as K_β increases, a smaller distance is covered within a time interval when micro-inertia goes up. This, can be seen in figure 10 in which the slopes of the straight lines corresponding to damage unloading waves are much greater for $K_\beta = 400$ than for $K_\beta = 1$, leaving wider zones in which $\widetilde{\mathcal{D}}$ and hence $\mathcal{D}$ can go to unity.

6.2 Kalthoff-Winkler test

We now move on to two-dimensional problems by first considering the Kalthoff-Winkler test [24] that consists in impacting a pre-notched specimen with a projectile to generate dynamic shear failure.

Given the symmetry of the considered problem, the numerical model is based on the setting depicted in figure 11a. The compressive load generated by the projectile is modeled by a Dirichlet boundary condition on the velocity that is purely horizontal on the bottom-left part of the domain. Symmetry is enforced on the bottom boundary and homogeneous Neumann boundary conditions are considered elsewhere.

The initial crack is modeled with one row of finite volume cells with initial data $\mathcal{D} = \widetilde{\mathcal{D}} = 0.95$. Notice that the mesh is locally refined (see figure 11b) in order to have an initial crack width of 0.5 mm and to better capture the solution in the zone where the crack propagates. The unstructured mesh is thus made of approximately 18000 quadrilateral cells of minimal edge length $h_{min} = 0.2$ mm. For this problem, the second-order in space flux difference splitting scheme presented in section 5 is used.

Plane strains are assumed, AT1 model is selected with the exponential coefficient set to $q = 8$, and the material parameters used, consistent with [5], are given in table 2. As can be seen, the characteristic length is such that

E (GPa)	ρ (kg·m^{-3})	ν	$\eta_{\mathscr{D}}$ (Pa·s)	ℓ_0 (m)	G_c (Pa)	λ (Pa)
190	8000	0.3	5×10^{-5}	3.9×10^{-4}	2.213×10^{4}	1×10^{3}

Table 2: Material parameters used for the Kalthoff-Winkler test.

$\ell_0 \approx 2h_{min}$.

First, figure 12 shows isovalues of the damage variable $\mathcal{D}$ and the hydrostatic pressure $p = \frac{1}{3}\operatorname{tr}\boldsymbol{\sigma}$. The tensile wave resulting from the reflection of the initial compression wave on the right free boundary can be seen in figure 12a. At that time, damage has only increased in the initial crack to get closer

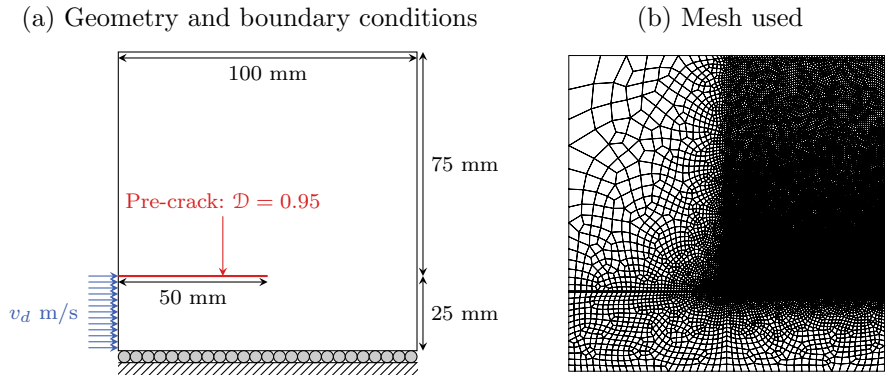


Figure 11: Geometry, boundary conditions and mesh used for the numerical modeling of the Kalthoff-Winkler test

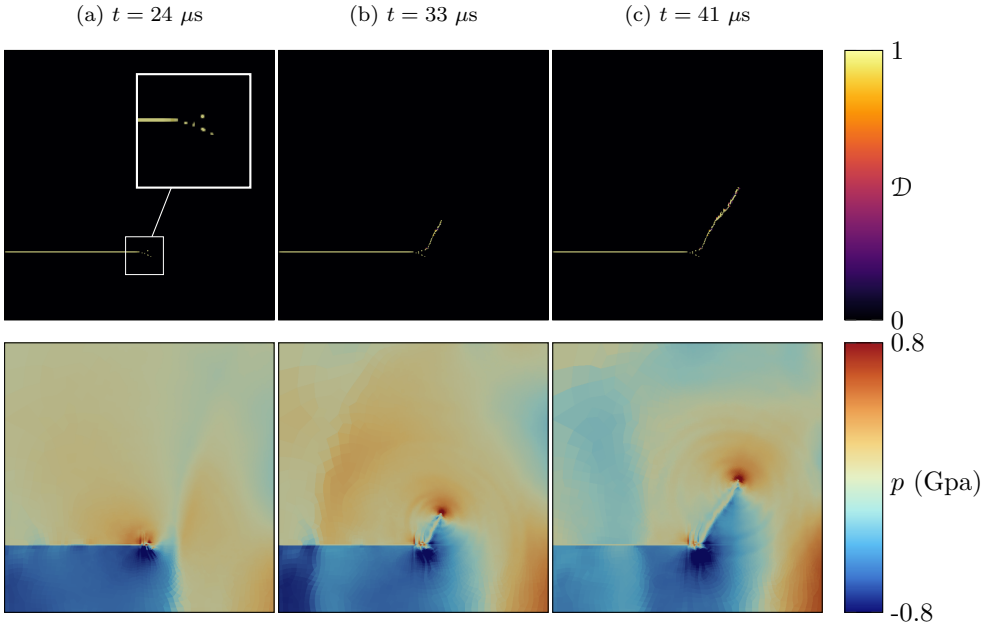


Figure 12: Damage variable and hydrostatic pressure in the domain at three different times. AT1 model, exponential coefficient $q = 8$ and micro-inertia factor $K_\beta = 1$.

to one, and in a few cells near the crack tip (see the magnified zone in the figure). This scattered evolution of damage is due to high strain amplitudes in some finite volumes that can most likely be removed with mesh refinement.

The actual propagation of the initial crack starts with the passage of the reflected tensile wave at the crack tip as can be seen in figure 12b. Indeed, the

crack tip has moved compared to the previous time, thus generating acoustic waves that can be distinguished by circular shades in the isovalues of p in the vicinity of the crack tip.

In figure 12c, the previously left-going tensile wave has been reflected as a compression wave that propagates towards the crack that continued advancing in the medium. This wave will eventually interact with the crack without stopping its progression as it is the case for many other waves resulting from multiple reflections of acoustic waves on the boundaries.

As a result, the crack tip reaches the right boundary of the domain as shown in figure 13, in which the final crack path can be seen for two different values of micro-inertia. Figure 13 also shows that micro-inertia has almost no effect

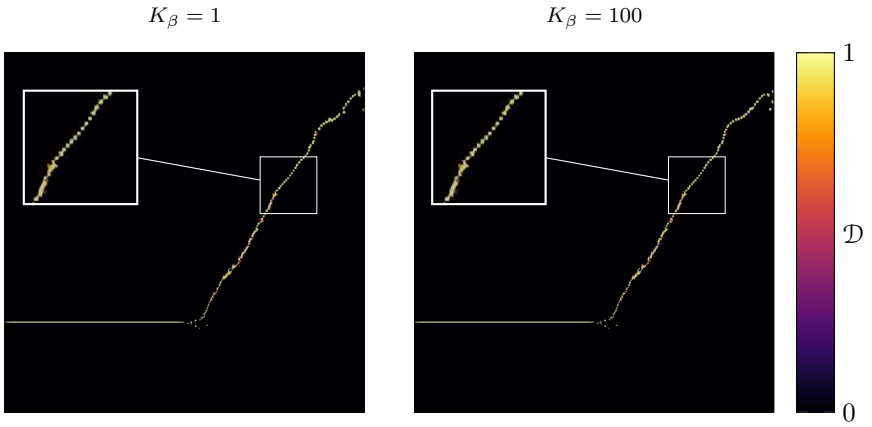


Figure 13: Final crack paths resulting from finite volume computations for two values of the micro-inertia factor K_β

for this benchmark. On the one hand, in contrast with the one-dimensional results presented before, the crack width is not larger when micro-inertia is increased. This could, however, not be the case if a finer mesh, leading to a higher number of cells in the characteristic length ℓ_0, was used. On the other hand, the trajectories followed by the crack tip only exhibit differences in final times.

This observation is confirmed in figure 14, where the horizontal and vertical coordinates of the crack tip are tracked over time for several values of the micro-inertia factor. Those curves have been obtained using the software ParaView [21] to isolate the crack namely, the set of finite volume cells contained in the subdomain $y \geq 25$ mm in which $\mathcal{D} \geq 0.98$, and extract at each time the position of its cell center furthest from the initial crack tip. The collected data are then filtered in order to only keep time steps at which the position of the crack tip has changed with respect to the previous ones. As the reader can see, horizontal (red) and vertical (blue) positions of the crack tip are identical

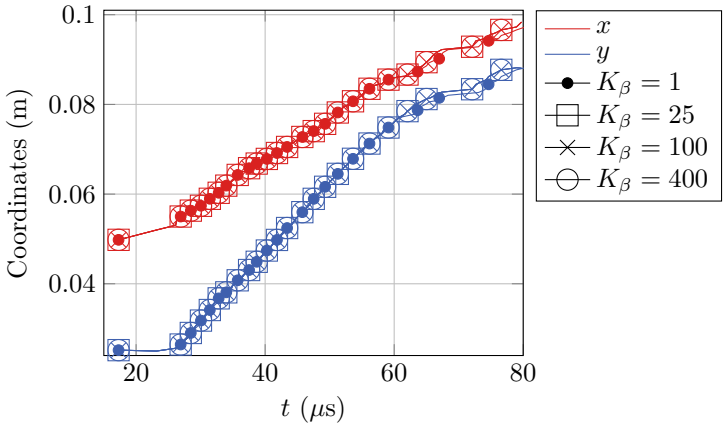


Figure 14: Crack tip coordinates within the domain with respect to physical time. Horizontal positions are depicted in red and vertical ones in blue.

until the time $t = 60\mu$s, after which the tip path differs with $K_\beta = 1$ differs from the others although mechanical quantities ($\boldsymbol{\varepsilon}$ and $\boldsymbol{\sigma}$) are very close in every simulations.

We now propose to look at the influence of micro-inertia by focusing on the variables $\beta\alpha$ and $\alpha = \dot{\widetilde{\mathcal{D}}}$. Generally speaking, and neglecting the numerical diffusion that may be involved by situations such that $c_{\mathcal{D}} \neq c_p(\mathcal{D})$, the former variable must be insensitive to K_β for it belongs to *conserved quantities*. However, this is not the case for $\dot{\widetilde{\mathcal{D}}}$ that directly results from division of a conserved quantity by the micro-inertia parameter, which monotonically increases with the micro-inertia factor according to equation (60), which is recalled here for convenience:

$$\beta = K_\beta \frac{\rho G_c \ell_0}{2c_w \left(\frac{4}{3}\mu + \kappa\right)}$$

As a consequence, for a given $\beta\alpha$, $\dot{\widetilde{\mathcal{D}}}$ decreases as β increases. This eventually leads to smaller values of $\mathcal{D}$ which in turn minimize the yield function (34) through the penalty term $\frac{\partial g}{\partial \mathscr{D}}$. As a result, the evolution of $\widetilde{\mathcal{D}}$ – and not of $\mathscr{D}$ – is "slowed down" by micro-inertia, as could be expected. The above discussion is illustrated in figure 15, in which the isovalues of $\beta\alpha$ and $\widetilde{\mathcal{D}}$ computed with two different values of micro-inertia are shown at time $t = 54$ μs. As can be seen, the quantity $\beta\alpha$ does not exhibit significant influence of micro-inertia near the crack tip. However, according to the above discussion, the auxiliary damage field $\widetilde{\mathcal{D}}$ is much lower in the same region when K_β increases.

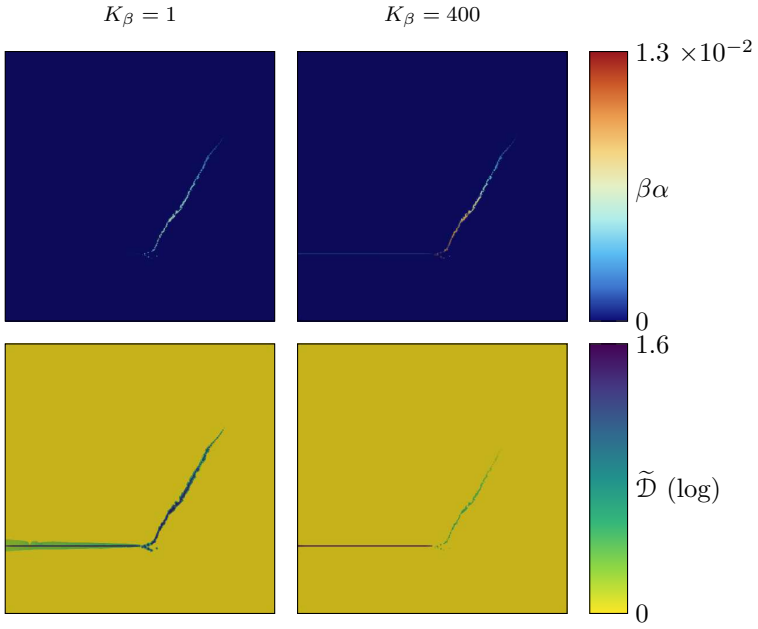


Figure 15: Plot of maps of $\beta\alpha$ and $\widetilde{\mathcal{D}}$ computed at time $t = 54$ μs with two different values of the micro-inertia factor.

6.3 Crack branching problem

The last benchmark of that paper considers a pre-notched rectangular plate suddenly submitted to tensile loads on its top and bottom boundaries as depicted in figure 16a. This study aims at illustrating the ability of the proposed model to capture crack branching for one expects that the solution consists in a first stage during which the initial crack propagates in the bulk following a straight line and eventually branches into two cracks [26]. The problem is here studied under the plane strain assumption and the initial crack is modeled as before by damage quantities with values $\widetilde{\mathcal{D}} = \mathcal{D} = 0.95$ in one row of cells. A structured mesh made of 140×119 quadrangular elements, that is finer and Cartesian in the crack propagation zone is used. This space discretization, shown in figure 16b, leads to the minimum edge length $h_{min} = 0.4$ mm$\approx \ell_0$.

As for Kalthoff's test, material parameters consistent with [5] have been used (see table 3). The AT2 model is used with the exponential coefficient set

E (GPa)	ρ (kg·m^{-3})	ν	$\eta_{\mathscr{D}}$ (Pa·s)	ℓ_0 (m)	G_c (Pa)	λ (Pa)
32	2450	0.2	5×10^{-5}	5×10^{-4}	3	1×10^{3}

Table 3: Material parameters used for the crack-branching test.

(a) Geometry and boundary conditions (b) Mesh used

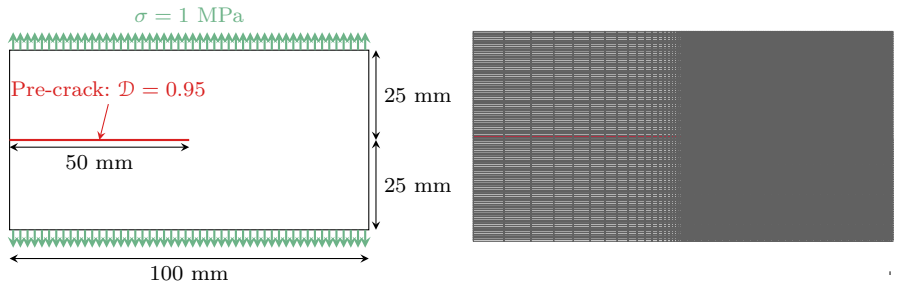


Figure 16: Geometry, boundary conditions and mesh used for the crack branching problem

to $q = 8$.

In this problem, tensile, compression and unloading waves as well as shear waves interact downstream the crack tip, thus generating crack propagation and branching. In contrast, the damage state along the symmetry line upstream the crack tip acts as a free boundary reflecting loading waves as unloading ones. Analyzing wave propagation and its consequences on damage evolution is not an easy task for that problem mainly for two reasons: 1/ the moving crack tip generates acoustic waves that are added to those coming from boundary conditions; 2/ the use of AT2 model, in which no purely elastic phase exists, instantaneously affects the damage field, and hence the wave speeds.

The numerical solution obtained for the micro-inertia factor value $K_\beta = 1$ is studied in terms of damage and hydrostatic pressure isovalues in figure 17 at several times. The first row in the figure shows the fields after the crack tip propagation due to tension at the center of the domain started. The wave fronts that can be seen in the hydrostatic isovalues correspond to tensile waves propagating toward the symmetry line.

After those waves interacted to generate tensile waves of higher amplitude propagating towards the top and bottom boundaries downstream the crack tip (see the second row in figure 17), branching has occurred. The computation then continues until the cracks reach the right end of the domain. At that time, plenty of waves propagate within the domain without creating new cracks.

The influence of micro-inertia is next shown in figure 18, in which the final crack paths computed with several values of the micro-inertia factor are depicted for comparison purpose.

As can be seen, the influence of micro-inertia on branching initiation is quasi-insignificant as indicates the horizontal dashed line in the figure. This result differs from the observation made in [53], for which micro-inertia can significantly delay the branching, which suggests that micro-inertia due to the damage gradient plays a very important role. Note also that “microbranchings” of more or less importance are observed in both solutions before the main

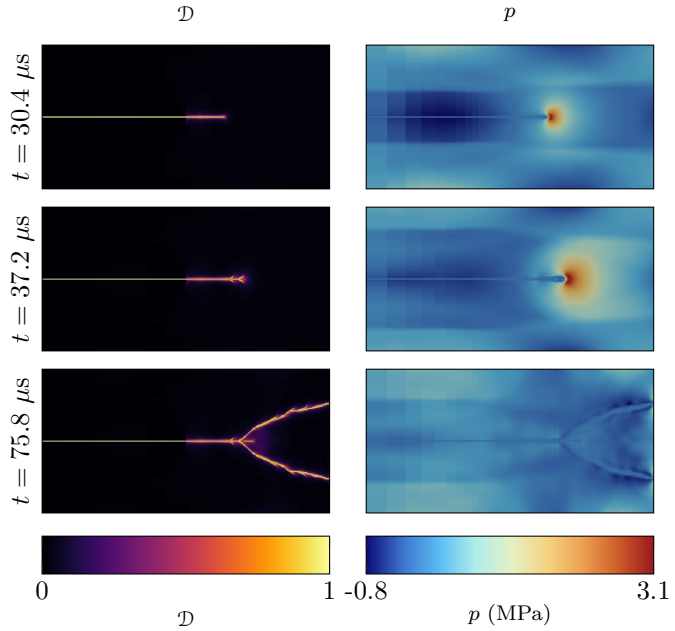


Figure 17: Isovalues of damage variable $\mathcal{D}$ and hydrostatic pressure in the medium at several times up to branching occurance (micro-inertia factor set to $K_\beta = 1$).

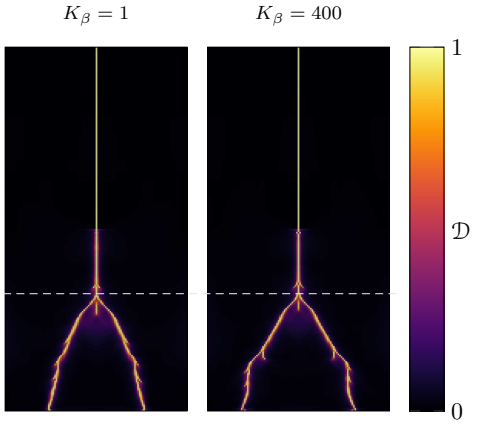


Figure 18: Damage profiles for the crack-branching problem for two values of the micro-inertia factor K_β.

branching occurs. In particular, a very small bifurcation can be seen near the tip of the pre-crack for $K_\beta = 400$ but not for $K_\beta = 1$.

Next, as already observed on the Kalthoff-Winkler test, micro-inertia doesn't influence the crack thickness in two space dimensions unlike in the one-dimensional multifragmentation test. However, the crack paths obtained can significantly differ depending on the value of the micro-inertia factor.

At last, it must be emphasized that the use of the AT2 model, without purely elastic phase, leads to elastic wave speeds that decrease everywhere in the domain after the first wave reflection. In such situations, $c_{\mathcal{D}}$ becomes the critical wave speed in the case $K_\beta = 1$ but not necessarily for $K_\beta = 400$ (it actually depends on the load amplitude). As a result, numerical diffusion of elastic waves, which highly drive the evolution of damage, can be very different from one value of micro-inertia to another. This point represents a limit of the model and should be the object of future works. The presented results nevertheless highlight the ability of the derived model to describe crack branching, which was the purpose of that benchmark.

7 Conclusion

In this paper, an extension of the hyperbolic model presented in [14] for one-dimensional problems to multi-dimensional ones has been proposed. After describing the thermodynamically-consistent constitutive model in section 2, and in particular the deviatoric/hydrostatic additive split of the elastic energy density considered to model the unilateral effect, local equations have been derived by means of Hamilton's variational principle in section 3. According to the extended Lagrangian methodology, a two-field formulation is constructed in which non-local damage terms, namely gradient and micro-inertia terms, involve an auxiliary non-dissipative damage variable. Irreversible processes are then considered by means of a rate-dependent damage evolution law for versatility though the extension to rate-independent models is possible. However, in contrast to the original formulation, use is here made of a *relaxed damage variable* $\mathscr{D} \geq 0$ in order to ensure the damage boundedness $\mathcal{D} < 1$ without external constraint or penalty terms. Both variables are related through an exponential-based function.

The proof of unconditional hyperbolicity carried out in section 4 allows the implementation of finite volume schemes, the one considered in that work being presented in section 5. This computational framework has first been illustrated on a one-dimensional multifragmentation problem. Convergence has then been shown in terms of the mesh size as well as of the parameter involved in the exponential change of variable, in such a way that the latter is not arbitrary but must rather be sufficiently large. In addition, an analysis of the effects of micro-inertia has been carried out, leading to the highlighting of the oscillating nature of the rate of change of the auxiliary damage and of the existence of damage unloading waves. Next, numerical results on two-dimensional benchmarks have proved that the model is able to describe crack propagation with realistic paths while capturing waves and crack branching.

As discussed at the end of section 6.3, the choice made to determine the value of the micro-inertia parameter can lead to situations such that damage waves propagate faster than elastic ones. This point, which is out of the scope of the present paper, must be the object of future works, ideally based on experimental researches for which evidences of damage waves would be of great help for the estimation of micro-inertia in brittle materials.

Acknowledgments

For the purpose of Open Access, a CC-BY public copyright license has been applied by the authors to the present document and will be applied to all subsequent versions up to the Author Accepted Manuscript arising from this submission.

References

1. Ambrosio, L., Tortorelli, V.M.: Approximation of functional depending on jumps by elliptic functional via t-convergence. Communications on Pure and Applied Mathematics **43**(8), 999–1036 (1990). DOI https://doi.org/10.1002/cpa.3160430805
2. Amor, H., Marigo, J.J., Maurini, C.: Regularized formulation of the variational brittle fracture with unilateral contact: Numerical experiments. Journal of the Mechanics and Physics of Solids **57**(8), 1209–1229 (2009)
3. Bažant, Z.P., Belytschko, T.B., Chang, T.P., et al.: Continuum theory for strain-softening. Journal of Engineering Mechanics **110**(12), 1666–1692 (1984)
4. Belytschko, T., Bažant, Z.P., Yul-Woong, H., Ta-Peng, C.: Strain-softening materials and finite-element solutions. Computers & Structures **23**(2), 163–180 (1986). DOI https://doi.org/10.1016/0045-7949(86)90210-5. URL https://www.sciencedirect.com/science/article/pii/0045794986902105
5. Borden, M., Verhoosel, C., Scott, M., Hughes, T., Landis, C.: A phase-field description of dynamic brittle fracture. Computer Methods in Applied Mechanics and Engineering **217-220**, 77–95 (2012). DOI 10.1016/j.cma.2012.01.008
6. Bourdin, B., Francfort, G., Marigo, J.J.: Numerical experiments in revisited brittle fracture. Journal of the Mechanics and Physics of Solids **48**(4), 797–826 (2000). DOI https://doi.org/10.1016/S0022-5096(99)00028-9
7. Bourdin, B., Marigo, J.J., Maurini, C., Sicsic, P.: Morphogenesis and propagation of complex cracks induced by thermal shocks. Phys. Rev. Lett. **112**, 014301 (2014). DOI 10.1103/PhysRevLett.112.014301
8. Chevaugeon, N., Moës, N.: Lipschitz regularization for fracture: The lip-field approach. Computer Methods in Applied Mechanics and Engineering **402**, 115644 (2022). DOI https://doi.org/10.1016/j.cma.2022.115644. A Special Issue in Honor of the Lifetime Achievements of J. Tinsley Oden
9. Colella, P.: Multidimensional upwind methods for hyperbolic conservation laws. Journal of Computational Physics **87**(1), 171–200 (1990). DOI https://doi.org/10.1016/0021-9991(90)90233-Q
10. Curnier, A., He, Q.C., Zysset, P.: Conewise linear elastic materials. Journal of Elasticity **37**, 1–38 (1994)
11. De Borst, R., Benallal, A., Heeres, O.: A gradient-enhanced damage approach to fracture. Le Journal de Physique IV **6**(C6), 491–512 (1996)
12. Dhaouadi, F., Favrie, N., Gavrilyuk, S.: Extended lagrangian approach for the defocusing nonlinear schrödinger equation. Studies in Applied Mathematics **142**(3), 336–358 (2019)

13. Favrie, N., Gavrilyuk, S.: A rapid numerical method for solving serre–green–naghdi equations describing long free surface gravity waves. Nonlinearity **30**(7), 2718 (2017)
14. Favrie, N., Renaud, A., Kondo, D.: Hyperbolic modeling of gradient damage and one-dimensional finite volume simulations. Computer Methods in Applied Mechanics and Engineering **419**, 116643 (2024). DOI https://doi.org/10.1016/j.cma.2023.116643
15. Forest, S.: Micromorphic approach for gradient elasticity, viscoplasticity, and damage. Journal of Engineering Mechanics **135**(3), 117–131 (2009)
16. François, M.L.: A damage model based on kelvin eigentensors and curie principle. Mechanics of materials **44**, 23–34 (2012)
17. Frémond, M., Nedjar, B.: Damage, gradient of damage and principle of virtual power. International Journal of Solids and Structures **33**(8), 1083–1103 (1996). DOI https://doi.org/10.1016/0020-7683(95)00074-7
18. Geromel Fischer, A., Marigo, J.J.: Gradient damage models applied to dynamic fragmentation of brittle materials: A. geromel fischer, j.-j. marigo. International Journal of Fracture **220**(2), 143–165 (2019)
19. Hai, L., Wu, J.Y., Li, J.: A phase-field damage model with micro inertia effect for the dynamic fracture of quasi-brittle solids. Engineering Fracture Mechanics **225**, 106821 (2020). DOI https://doi.org/10.1016/j.engfracmech.2019.106821. URL https://www.sciencedirect.com/science/article/pii/S0013794419307702
20. Halphen, B., Nguyen, Q.: On generalized standard materials. J Mec **14**, 39–63 (1975)
21. Henderson, A., Ahrens, J., Law, C.: The Paraview Guide, vol. 230 (2004)
22. Heuzé, T.: Simulation of impacts on elastic-viscoplastic solids with the flux-difference splitting finite volume method applied to non-uniform quadrilateral meshes. Advanced Modeling and Simulation in Engineering Sciences **5**(1) (2018). DOI 10.1186/s40323-018-0101-z
23. Kachanov, L.: On creep rupture time. Izv. Acad. Nauk SSSR, Otd. Techn **8**, 26–31 (1958)
24. Kalthoff, J.: Modes of dynamic shear failure in solids. International Journal of Fracture **101**, 1–31 (2000)
25. Kamensky, D., Moutsanidis, G., Bazilevs, Y.: Hyperbolic phase field modeling of brittle fracture: Part i—theory and simulations. Journal of the Mechanics and Physics of Solids **121**, 81–98 (2018)
26. Kobayashi, A., Wade, B., Bradley, W., Chiu, S.: Crack branching in homalite-100 sheets. Engineering Fracture Mechanics **6**(1), 81–92 (1974). DOI https://doi.org/10.1016/0013-7944(74)90048-4
27. Langenfeld, K., Kurzeja, P., Mosler, J.: On the curvature dependence of gradient damage models: Control and opportunities. Computer Methods in Applied Mechanics and Engineering **410**, 115987 (2023). DOI https://doi.org/10.1016/j.cma.2023.115987. URL https://www.sciencedirect.com/science/article/pii/S004578252300110X
28. LeVeque, R.J.: Wave propagation algorithms for multidimensional hyperbolic systems. Journal of Computational Physics **131**(2), 327–353 (1997). DOI https://doi.org/10.1006/jcph.1996.5603. URL https://www.sciencedirect.com/science/article/pii/S002199919695603X
29. LeVeque, R.J.: Nonlinear conservation laws and finite volume methods. In: Computational methods for astrophysical fluid flow, pp. 1–159. Springer (1998)
30. Li, T., Marigo, J.J., Guilbaud, D., Potapov, S.: Gradient damage modeling of brittle fracture in an explicit dynamics context. International Journal for Numerical Methods in Engineering **108**(11), 1381–1405 (2016). DOI https://doi.org/10.1002/nme.5262
31. Lorentz, E., Andrieux, S.: A variational formulation for nonlocal damage models. International journal of plasticity **15**(2), 119–138 (1999)
32. Lorentz, E., Benallal, A.: Gradient constitutive relations: numerical aspects and application to gradient damage. Computer Methods in Applied Mechanics and Engineering **194**(50), 5191–5220 (2005). DOI https://doi.org/10.1016/j.cma.2004.12.016
33. Mersel, L., Bouda, P., Germain, J., Réthoré, J.: Dynamic damage modelling through phase-field approaches: assessment, critical analysis and comparison. Comptes Rendus. Mécanique **353**, 687–724 (2025). DOI 10.5802/crmeca.297
34. Miehe, C., Hofacker, M., Schänzel, L.M., Aldakheel, F.: Phase field modeling of fracture in multi-physics problems. part ii. coupled brittle-to-ductile failure criteria and crack

propagation in thermo-elastic–plastic solids. Computer Methods in Applied Mechanics and Engineering **294**, 486–522 (2015). DOI https://doi.org/10.1016/j.cma.2014.11.017
35. Miehe, C., Welschinger, F., Hofacker, M.: Thermodynamically consistent phase-field models of fracture: Variational principles and multi-field fe implementations. International Journal for Numerical Methods in Engineering **83**(10), 1273–1311 (2010). DOI https://doi.org/10.1002/nme.2861
36. Moreau, K., Moes, N., Picart, D., Stainier, L.: Explicit dynamics with a non-local damage model using the thick level set approach. International Journal for Numerical Methods in Engineering **102** (2014). DOI 10.1002/nme.4824
37. Moës, N., Lé, B., Stershic, A.: Fragmentation analysis of a bar with the lip-field approach. Mechanics of Materials **172**, 104365 (2022). DOI https://doi.org/10.1016/j.mechmat.2022.104365
38. Moës, N., Stolz, C., Bernard, P.E., Chevaugeon, N.: A level set based model for damage growth: The thick level set approach. International Journal for Numerical Methods in Engineering **86**(3), 358–380 (2011). DOI https://doi.org/10.1002/nme.3069
39. Nguyen, Q.S., Andrieux, S.: The non-local generalized standard approach: a consistent gradient theory. Comptes Rendus Mécanique **333**(2), 139–145 (2005). DOI https://doi.org/10.1016/j.crme.2004.09.010
40. Parrinello, A.: A rate-pressure-dependent thermodynamically-consistent phase field model for the description of failure patterns in dynamic brittle fracture. Ph.D. thesis, University of Oxford (2017)
41. Peerlings, R.H.J., de Borst, R., Brekelmans, W.A.M., Geers, M.G.D.: Gradient-enhanced damage modelling of concrete fracture. Mechanics of Cohesive-frictional Materials **3**(4), 323–342 (1998)
42. Pham, K., Amor, H., Marigo, J.J., Maurini, C.: Gradient damage models and their use to approximate brittle fracture. International Journal of Damage Mechanics **20**, 618–652 (2010). DOI 10.1177/1056789510386852
43. Pham, K., Marigo, J.J.: Approche variationnelle de l'endommagement : I. les concepts fondamentaux. Comptes Rendus Mécanique **338**(4), 191–198 (2010). DOI https://doi.org/10.1016/j.crme.2010.03.009
44. Pham, K., Marigo, J.J.: Approche variationnelle de l'endommagement : Ii. les modèles à gradient. Comptes Rendus Mécanique **338**(4), 199–206 (2010). DOI https://doi.org/10.1016/j.crme.2010.03.012
45. Pijaudier-Cabot, G., Bažant, Z.P.: Nonlocal damage theory. Journal of engineering mechanics **113**(10), 1512–1533 (1987)
46. Plohr, B.J., Sharp, D.H.: A conservative eulerian formulation of the equations for elastic flow. Advances in Applied Mathematics **9**(4), 481 – 499 (1988)
47. Renaud, A., Heuzé, T., Stainier, L.: On loading paths followed inside plastic simple waves in two-dimensional elastic-plastic solids. Journal of the Mechanics and Physics of Solids **143**, 104064 (2020). DOI 10.1016/j.jmps.2020.104064
48. Renaud, A., Heuzé, T., Stainier, L.: The discontinuous galerkin material point method for variational hyperelastic–plastic solids. Computer Methods in Applied Mechanics and Engineering **365**, 112987 (2020). DOI https://doi.org/10.1016/j.cma.2020.112987
49. Svolos, L., Mourad, H.M., Manzini, G., Garikipati, K.: A fourth-order phase-field fracture model: Formulation and numerical solution using a continuous/discontinuous galerkin method. Journal of the Mechanics and Physics of Solids **165**, 104910 (2022). DOI https://doi.org/10.1016/j.jmps.2022.104910
50. Sweby, P.K.: High resolution schemes using flux limiters for hyperbolic conservation laws. SIAM Journal on Numerical Analysis **21**(5), 995–1011 (1984). DOI 10.1137/0721062
51. Tanné, E., Li, T., Bourdin, B., Marigo, J.J., Maurini, C.: Crack nucleation in variational phase-field models of brittle fracture. Journal of the Mechanics and Physics of Solids **110**, 80–99 (2018)
52. Toro, E.F.: Riemann solvers and numerical methods for fluid dynamics: a practical introduction. Springer Science & Business Media (2013)
53. Wang, Z., Shedbale, A.S., Kumar, S., Poh, L.H.: Localizing gradient damage model with micro inertia effect for dynamic fracture. Computer Methods in Applied Mechanics and Engineering **355**, 492–512 (2019). DOI https://doi.org/10.1016/j.cma.2019.06.029

54. Zeng, Z., Ni, R., Zhang, X., Liu, Y.: An explicit phase field material point method for modeling dynamic fracture problems. International Journal for Numerical Methods in Engineering **124**(12), 2680–2708 (2023). DOI https://doi.org/10.1002/nme.7231
55. Zhang, Z., Qiu, Y., Hu, Z., Ye, H., Zhang, H., Zheng, Y.: Explicit phase-field total lagrangian material point method for the dynamic fracture of hyperelastic materials. Computer Methods in Applied Mechanics and Engineering **398**, 115234 (2022). DOI https://doi.org/10.1016/j.cma.2022.115234

Supplementary Files

This is a list of supplementary files associated with this preprint. Click to download.

- code1Dmultifragmentation.zip